

RI 9271

RI 9271

REPORT OF INVESTIGATIONS/1989

Collimated Abrasive Water-Jet Behavior

By David E. Swanson

BUREAU OF MINES



UNITED STATES DEPARTMENT OF THE INTERIOR

Mission: As the Nation's principal conservation agency, the Department of the Interior has responsibility for most of our nationally-owned public lands and natural and cultural resources. This includes fostering wise use of our land and water resources, protecting our fish and wildlife, preserving the environmental and cultural values of our national parks and historical places, and providing for the enjoyment of life through outdoor recreation. The Department assesses our energy and mineral resources and works to assure that their development is in the best interests of all our people. The Department also promotes the goals of the Take Pride in America campaign by encouraging stewardship and citizen responsibility for the public lands and promoting citizen participation in their care. The Department also has a major responsibility for American Indian reservation communities and for people who live in Island Territories under U.S. Administration.

Report of Investigations 9271

Collimated Abrasive Water-Jet Behavior

By David E. Swanson

UNITED STATES DEPARTMENT OF THE INTERIOR
Manuel Lujan, Jr., Secretary

BUREAU OF MINES
T S Ary, Director

Library of Congress Cataloging in Publication Data:

Swanson, David E.

Collimated abrasive water-jet behavior.

(Report of investigations; 9271)

Bibliography: p. 42

Supt. of Docs. no.: I 28.23:9271.

1. Hydraulic mining. 2. Jet cutting. 3. Water jet. 4. Abrasives. I. Title. II. Series: Report of investigations (United States. Bureau of Mines); 9271.

TN23.U43 [TN278] 622 s [622'.028] 89-600004

CONTENTS

	<i>Page</i>
Abstract	1
Introduction	2
Background	2
Process description	3
Experimental program	5
Procedures	5
Equipment	9
Analytical methods	13
Results	16
General behavior	16
Visual form of jet	16
Circulation zones within collimating pipe	21
Induction flows	22
Wear to collimating pipes	22
Impingement of abrasives	24
Response to independent variables	30
Nozzle pressure	30
Collimating pipe length	36
Collimating pipe internal diameter	38
Induction port position and size	40
Alignment of nozzle and collimating pipe	40
Collimating pipe material	40
Discussion	41
References	42
Appendix.—Symbol identification	43

ILLUSTRATIONS

1. Conventional method of abrasive mixing	2
2. Collimation method of abrasive mixing	3
3. Elements of collimated water-jet flow	4
4. Transparent tee for viewing mixing and entrainment	5
5. Single-exposure photographic techniques	6
6. Two-camera photographic techniques	7
7. Multiple-exposure photographic technique	7
8. Schematic of equipment layout	9
9. High-pressure pumping unit	10
10. High-efficiency water-jet nozzle	10
11. Abrasive induction probe	11
12. Experimental entrainment apparatus	12
13. Modified experimental entrainment apparatus	12
14. Water-jet expansion	17
15. Water-jet collimation in transparent tubing	18
16. Collimated abrasive water jet	19
17. Abrasive induction into water jet	21
18. Cumulative abrasive throughput versus pipe weight	23
19. Thickness profile of worn collimating pipes	24
20. Radial distribution of impact craters	26
21. Impact craters in polished steel plate	27
22. Radial position versus size of impact craters	29
23. Operating pressure versus nozzle discharge rate	30
24. Operating pressure versus induction line vacuum	32
25. Operating pressure versus reactive force, efflux velocity, and efflux power	33

ILLUSTRATIONS--Continued

	<i>Page</i>
26. Operating pressure versus composition by weight and composition by volume	35
27. Collimating pipe length versus reactive force, efflux velocity, and efflux power	37
28. Collimating pipe internal diameter versus abrasive flow rate	38
29. Collimating pipe internal diameter versus reactive force, efflux velocity, and efflux power	39
30. Efflux flow resulting from misalignment of nozzle and collimating pipe	41

TABLES

1. Physical properties of abrasives	11
2. Air density calculations	14
3. Collimating pipe wear and effects	22
4. Wear patterns in collimating pipes	23
5. Radial distribution of impact craters	25
6. Crater size data	28
7. Operating pressure and nozzle discharge properties	30
8. Operating pressure and collimated water-jet properties (no induction)	31
9. Operating pressure and collimated water-jet properties (air induction)	31
10. Operating pressure and collimated water-jet properties (air and abrasive induction)	31
11. Collimated water-jet composition by phase	34
12. Collimating pipe length and collimated water-jet properties	36
13. Collimating pipe internal diameter and collimated water-jet properties	38
14. Induction port position and collimated water-jet properties	40

UNIT OF MEASURE ABBREVIATIONS USED IN THIS REPORT

With Factors for Conversion to U.S. Customary Units

Abbreviation	Unit of measure	To convert to--	Multiply by--
°C	degree Celsius	degrees Fahrenheit	1.8 + 32
cm	centimeter	inches	.3937
cm ²	centimeter squared	inches squared	.1550
g	gram	pounds (avoirdupois)	.0022
g/cm ³	gram per cubic centimeter	pounds per cubic foot	62.427961
g/L	gram per liter	pounds per cubic foot	.06242621
g/s	gram per second	pounds per minute	.132
hp	horsepower	kilowatts	.7457
in	inch		
°K	degree Kelvin	degrees Fahrenheit	1.8 + 305
kg	kilogram	pounds (avoirdupois)	2.2046226
kg/s	kilogram per second	pounds (avoirdupois) per second	2.2
kPa	kilopascal	pounds per square inch	.1450
kW	kilowatt	horsepower	1.34102
L/s	liter per second	gallons per minute	15.85077
m	meter	feet	3.281
mg	milligram	pounds (avoirdupois)	.0000022
min	minute		
mm	millimeter	inches	.03937
mm ²	millimeter squared	square inches	.00155
mm Hg	millimeter of mercury	pounds per square inch	.0193368
MPa	megapascal	pounds per square inch	145.0
m/s	meter per second (time)	feet per second	3.281

UNIT OF MEASURE ABBREVIATIONS USED IN THIS REPORT--Continued

With Factors for Conversion to U.S. Customary Units

Abbre- viation	Unit of measure	To convert to--	Multiply by--
μ s	microsecond		
N	newton	pound force	.2248
pct	percent		
rad	radian	degrees	57.29577951
s	second (time)		
vol pct	volume percent		
wt pct	weight percent		
\$/kg	dollar per kilogram	dollars per pound	2.2
\$/m	dollar per meter	dollars per foot	3.281

COLLIMATED ABRASIVE WATER-JET BEHAVIOR

By David E. Swanson¹

ABSTRACT

The U.S. Bureau of Mines undertook a basic investigation of collimated abrasive water-jet behavior because a more complete understanding of the fundamental process may lead to further technical advances. Laboratory experiments used 2-mm water-jet nozzles and new entrainment apparatus to analyze collimated abrasive water jets operating under varied conditions. Maximum water pressure was 69 MPa to permit use of conventional hoses with a burst-to-operating-pressure ratio of 4. Nozzle and induction line pressures, abrasive induction rates, and jet reactive thrust forces were recorded for each operating condition. Average jet velocity and power were determined from component mass flow rates and reactive thrust force measurements. Relative velocity and cross-sectional distribution of abrasive particles were determined using impact analysis techniques. Other jet characteristics were determined photographically. Properties of free water jets, collimated water jets, and collimated air-water jets were determined for comparison.

¹Mining engineer, Twin Cities Research Center, U.S. Bureau of Mines, Minneapolis, MN.

INTRODUCTION

BACKGROUND

The presence of abrasive particles in a high-velocity water jet creates an abrasive slurry with cutting characteristics of potentially great importance to the mining industry. Abrasive water-jet (AWJ) rock-cutting techniques offer the following advantages over mechanical rock-cutting methods: (1) elimination of bits and bit wear, (2) dust reduction and suppression, (3) decreased equipment weight, (4) increased equipment mobility, (5) elimination of overbreak, (6) increased penetration per pass, (7) reduced risk of spark ignition, (8) clean, precision cutting, (9) selective removal of weaker rock, and (10) reduction of minimum-diameter drilling limitations.

Cutting performance with an AWJ is largely a function of the square of abrasive particle velocity (1-2);² therefore, it increases markedly with increasing particle velocity. Abrasives in a pressurized water slurry can be efficiently accelerated through a nozzle, but wear to nozzle and pump components discourages this practice (3). Processes that entrain abrasives into high-velocity water jets downstream of a primary nozzle must overcome efficiency problems in accelerating abrasives or use higher water pressures (3-4).

AWJ equipment design is evolving to improve cutting capabilities. In the conventional method of mixing abrasives into a water jet, a primary nozzle generates a high-velocity water jet and then a secondary nozzle merges abrasive particles and air with the water jet (fig. 1). In conventional systems, most abrasive particles bounce off the water jet into the walls of the secondary nozzle, and particles that do enter the water jet fail to penetrate its periphery (4). Exiting the secondary nozzle, average abrasive particle velocity is much less than the efflux water jet velocity of the primary nozzle. At 69-MPa operating pressure, average particle velocities for garnet and steel shot abrasives exiting a secondary nozzle are roughly 76 and 53 m/s, respectively (4), yet an efficient primary nozzle generates a water jet velocity of about 370 m/s.

To achieve abrasive velocities necessary for economical performance in surface scoring and cutting of thin, flat materials, conventional AWJ's operate at pressures ranging from 200 to 400 MPa. In an attempt to achieve acceptable cutting at lower operating pressures, conventional AWJ systems using multiple water jets at 138-MPa operating pressure have been tried in order to more efficiently entrain abrasives at the secondary nozzle (5).

As part of its program to advance mining technology, the U.S. Bureau of Mines developed collimated abrasive water-jet (CAWJ) techniques to cut hard rock using a 69-MPa operating pressure (6-9), because conventional AWJ technology is poorly suited for most mining applications. Working pressures above 69 MPa present numerous problems for mining applications (e.g.,

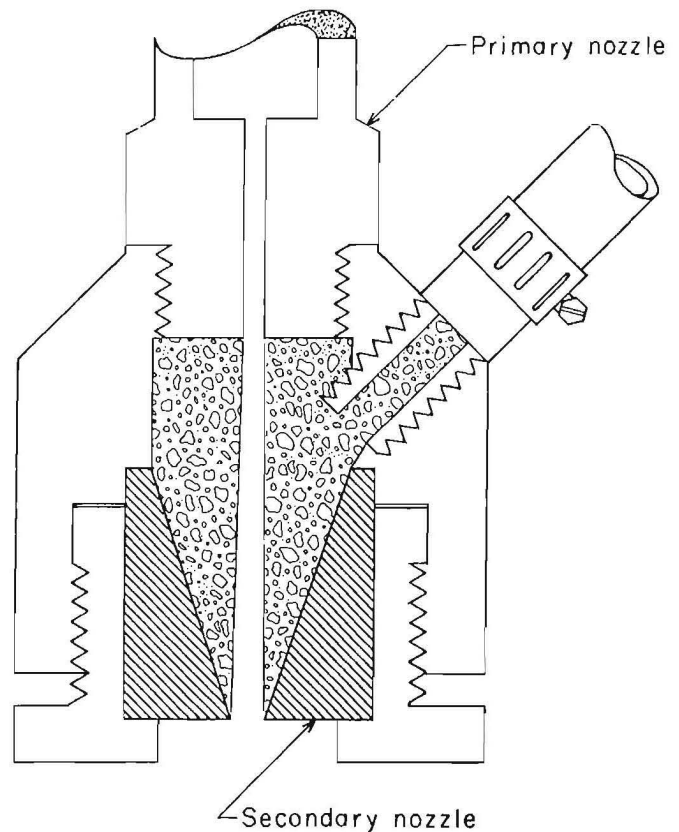


Figure 1.—Conventional method of abrasive mixing.

equipment is significantly more expensive and difficult to maintain, hoses and fittings restrict mobility because of limited flexibility and large bend radii, and increased working pressures present increased safety concerns for workers). CAWJ techniques entrain abrasives downstream of a primary nozzle without a secondary nozzle (fig. 2). Abrasive particles and air are mixed by entrainment into the axially flowing water jet within a straight section of pipe called a collimating pipe. Deflectors at the efflux end of the collimating pipe modify the CAWJ so that it can produce an enlarged opening in rock, enabling the collimating pipe to follow the water jet into the cut to create deep slots that are far beyond the penetration capability of nonadvancing jets (6). Using a low-cost, low-maintenance swivel, a deflector-modified CAWJ can drill holes of controllable diameter through both competent and unconsolidated rock (8).

The Bureau undertook the basic investigation of CAWJ behavior presented in this report to gain a more complete understanding of fundamental processes as a catalyst to future technical advancement. Using 2-mm water-jet nozzles and a new entrainment apparatus, the Bureau

²Italic numbers in parentheses refer to items in the list of references preceding the appendix.

PROCESS DESCRIPTION

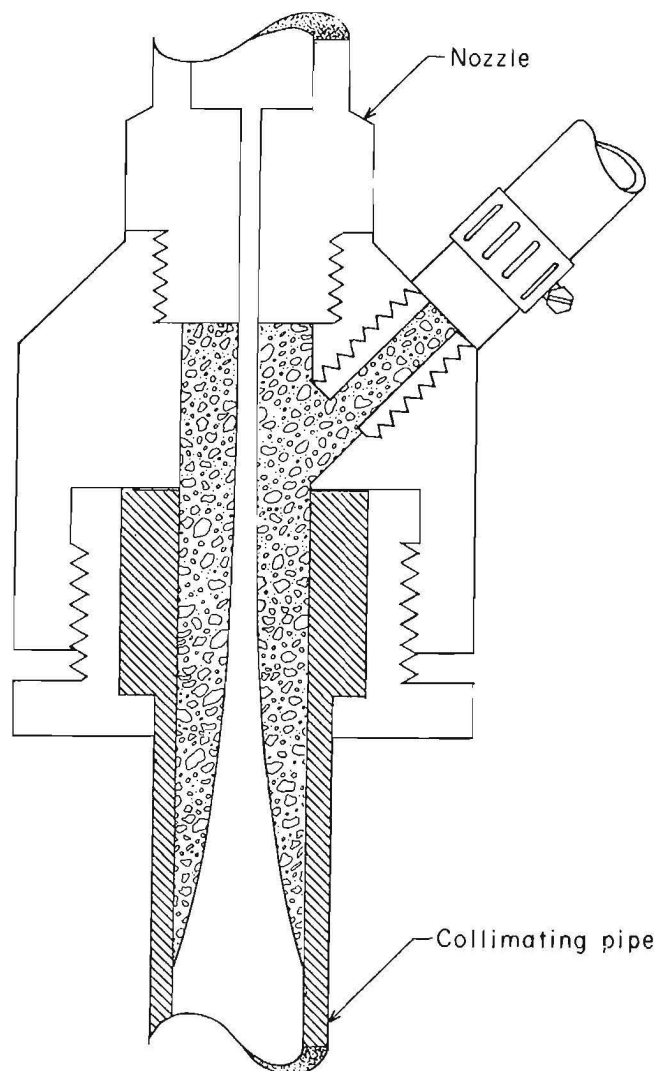


Figure 2.—Collimation method of abrasive mixing.

analyzed the CAWJ as it operated under various induction and collimating conditions. Because of the complexity of modeling three-phase flows, empirical approaches were undertaken in preference to purely theoretical methods. Analytical modeling of turbulent three-phase flows is characterized by attempts to equate complex formulas to experimental data. At this time, there are no practical analytical methods to acquire the information that was empirically obtained in the reported tests. Even the dynamic viscosity (a starting place in many flow calculations) cannot be accurately determined for high-velocity, turbulent three-phase flows by analytical methods.

In a CAWJ, acceleration of abrasive particles involves momentum transfer through mixing of the three-phase constituents: water, air, and abrasives. Figure 3 shows characteristic flow regions and flow patterns. The underlying hydrodynamic elements of the CAWJ are closely interrelated.

Potential pressure energy is converted to kinetic energy across the nozzle. The nozzle produces a high-velocity water jet directed along the central axis of a coaxially larger, constant-diameter collimating pipe. The water jet discharges from the nozzle as a continuous column of coherent water.

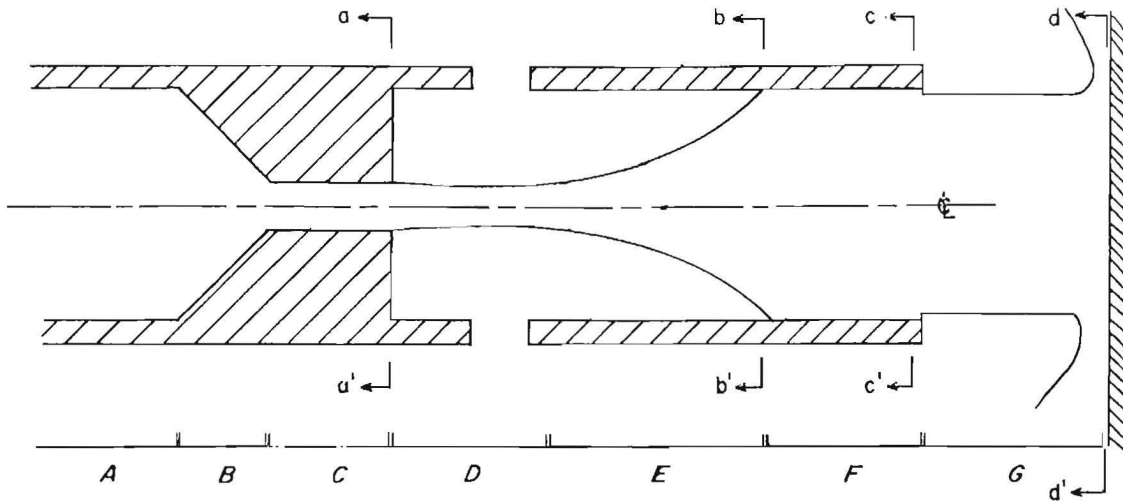
At the nozzle efflux plane, inertial effects prevent the water jet from immediately filling the collimating pipe, and the axial water jet travels through relatively stagnant surroundings.³ The flow separation is away from the collimating pipe interior walls and precludes a velocity loss in keeping with continuous fluid flow, whereas an increase in conduit area is accompanied by a proportional decrease in velocity (10).

In a collimating pipe with an internal diameter much greater than the nozzle orifice, the axial water jet accelerates the surrounding air in the fashion of a jet pump. Through viscous interaction, the peripheral fluids near the nozzle are drawn by the axial water jet down the collimating pipe.

Continuous evacuation near the nozzle creates a low-pressure region that generates an induction airflow. With ports in the collimating pipe near the nozzle, an induction flow of air from outside the entrainment apparatus delivers abrasive particles by suction pickup and pneumatic transport. Induction flow of air and abrasives is directed through a hose connected to the entrainment apparatus, and induction rates can be reduced by hose restrictions.

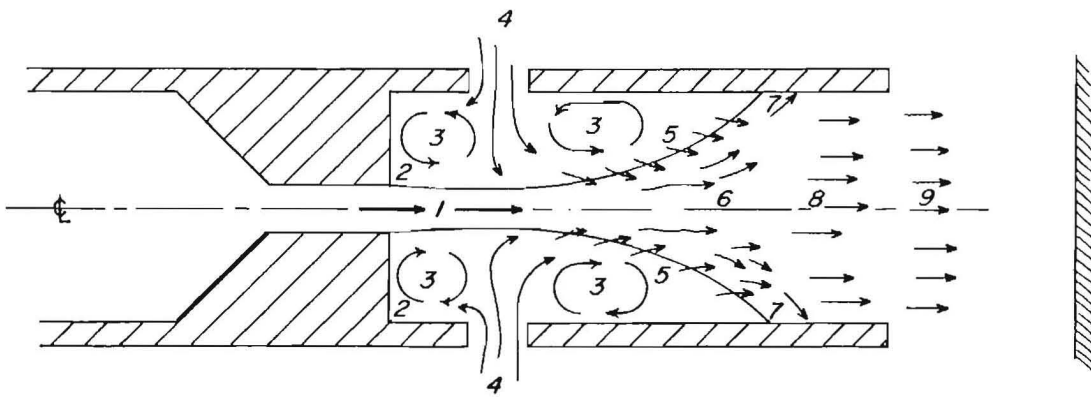
Confined within the collimating pipe and immediately downstream from the nozzle, an axial core of turbulent and coherent water is surrounded by a less turbulent annulus of air and abrasives. The water jet initially behaves like a free jet, spreading turbulence into and entraining its fluid surroundings. Jet flow is considered "free" if the jet cross-sectional area is less than 20 pct of the total cross-sectional area through which it is traveling (11). Entrainment (i.e., mass transfer across a boundary separating a turbulent region from an adjacent less-turbulent region) will be toward the more turbulent region (12). The rate of entrainment is related to the turbulence ratio of the axial (primary) to coaxial (secondary) flows.

³In this report, "axial" means centrally located within the collimating pipe.



KEY

- | | |
|--|---|
| <i>A</i> High-pressure water line | <i>aa'</i> Nozzle efflux plane and separation plane |
| <i>B</i> Convergent section of nozzle | <i>bb'</i> Reattachment plane |
| <i>C</i> Straight section of nozzle | <i>cc'</i> Collimating pipe efflux plane |
| <i>D</i> Induction and confluence zone | <i>dd'</i> Impingement plane |
| <i>E</i> Mixing region | ϕ Jet axis |
| <i>F</i> Collimated flow region | |
| <i>G</i> Efflux jet | |



KEY

- | |
|-------------------------------------|
| <i>1</i> Coherent water column flow |
| <i>2</i> Separation flow |
| <i>3</i> Circulation zones |
| <i>4</i> Induction flow |
| <i>5</i> Entrainment flow |
| <i>6</i> Mixing flow |
| <i>7</i> Reattachment flow |
| <i>8</i> Collimated flow |
| <i>9</i> Efflux flow |

Figure 3.-Elements of collimated water-jet flow. Top, flow regions; bottom, flow patterns.

Eddying at the water-jet exterior causes turbulent mixing of abrasive particles and air into the axial water jet. The entrainment interface expands both inward and outward until the collimating pipe is filled with a three-phase flow of air, abrasives, and water. Entrainment continues as long as a turbulence gradient persists between adjacent flow components.

Collimation occurs as the axial and coaxial flows combine to become a single flow. As the mixing region expands outward, wall separation for the axial flow decreases. Reattachment occurs where the expanding mixing region contacts the inner wall of the collimating pipe. Confined turbulent mixing continues to blend air, abrasives, and water downstream of the reattachment plane. Mixing reduces the cross-sectional variation of velocity and density within the collimating pipe to eliminate distinct axial maximums with downstream travel. Velocity and density losses along the axis coincide with gains at the periphery. Although a high degree of turbulence remains, collimation gives the resulting jet a unified flow direction dictated by the collimating pipe.

The velocity of a CAWJ traveling within a collimating pipe is conserved beyond that of water jets traveling through air (9). The collimating pipe prevents the reduction of flow density by limiting expansion and entrainment. Within the collimating pipe, the CAWJ is shielded from wind shear. Wall friction is minor because the highly turbulent flows have reduced viscous effects (13). Because frictional wall effects are less prominent in turbulent flows than in laminar flows, confined multiphase turbulent jets tend to be more uniform in cross-sectional velocity than more laminar analogues. The presence of solids in the CAWJ may additionally lower friction and turbulence intensity (14).

The CAWJ becomes a free jet when it exits the collimating pipe. Entrainment and diffusion processes may alter the CAWJ after it leaves the collimating pipe, but cutting is generally conducted within a limited standoff distance. Cutting occurs when the CAWJ impinges on a surface and is deflected. CAWJ cutting involves many mechanisms.

EXPERIMENTAL PROGRAM

PROCEDURES

Experiments were undertaken to determine the behavior of the CAWJ. Both general operating conditions and responses to changes in independent variables were analyzed. Maximum water pressure was limited to 69 MPa to permit the use of conventional high-pressure, flexible water hoses with a burst-pressure safety factor of 4. Nozzle orifice size, 2 mm, was periodically measured to assure consistency.

Jet flows were examined using several lighting and photographic techniques. To determine whether pressure pulsations were present in the nozzle efflux flow, the jet was examined under stroboscopic lighting of 1 to 417 flashes per second and by high-speed photography (15). To observe and photograph flow within collimating pipes, glass and high-vacuum-rated transparent polyurethane tubing were used in place of steel pipes (fig. 4). This substitution presented a formidable predicament; abrasives quickly abrade glass and plastic, making them nontransparent. To redress this difficulty, photography of flow in transparent tubing was limited to nonabrasive flows or flows in the first few seconds after the addition of abrasives.

To "stop" the motion of the jet and indicate structure, high-speed photographic methods were used. Photographic resolution of a fast-moving particle requires the exposure period to be as brief as the time it takes the particle to travel a distance corresponding to one-half its diameter; e.g., an exposure period of 1 μ s or briefer is necessary to resolve a 1-mm grain of sand traveling at 500 m/s. With camera shutters held open in a dark laboratory, exposure times of 0.8, 1.2, and 3.0 μ s were

controlled at the light source using singly pulsed stroboscopes. These durations represent the time interval over which one-third of peak light intensity was exceeded. For a single flash, peak intensity was approximately 18 million candela at a 1-m standoff.

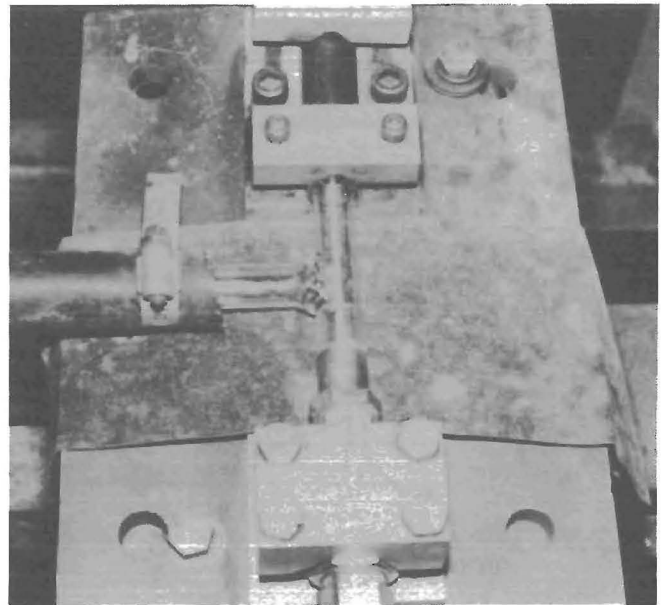


Figure 4.—Transparent tee for viewing mixing and entrainment.

Three illumination techniques (fig. 5) were used: back illumination with diffused light to give details of the jet interior, polariscopic back illumination to give details of the outer part of the flow, and frontal illumination for general information. With the jet positioned between crossed polarizers, objects that change the polarity of the transmitted light (e.g., water and birefringent quartz) appear brighter in photographs.

Using two cameras, simultaneous stereo and orthogonal photographs were taken to analyze water-jet structure (fig. 6). By exposing with a single flash, two cameras can obtain comparative perspectives of the jet at the same instant. Stereo images can enhance perception of depth, and orthogonal images can be used to triangulate radial positions.

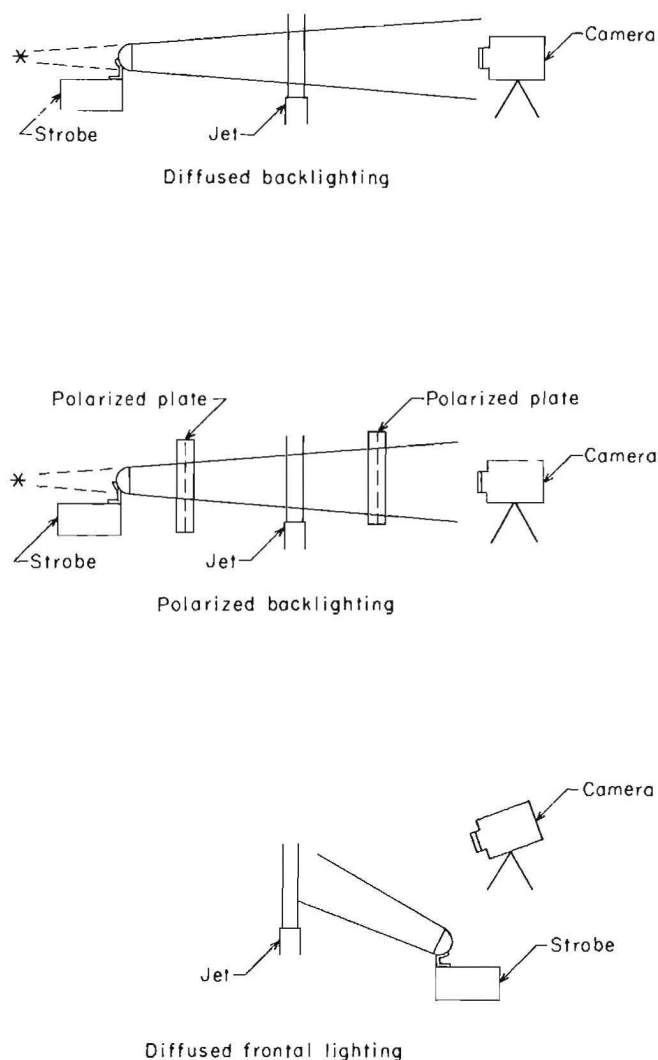


Figure 5.—Single-exposure photographic techniques.

Multiple-exposure photographs were taken to indicate abrasive particle direction in collimated efflux flows and to verify calculations of velocity. This technique (fig. 7) employed sequentially pulsed stroboscopes in a darkened laboratory with the camera shutter held open. Two stroboscopes were operated sequentially by separate electronic pulse generators to produce double-exposure photographs with accurate delay intervals between exposures. The first pulse generator was manually triggered, and it in turn activated both the first strobe and the second pulse generator. Using a variable delay feature, the second pulse generator was capable of controlled delay intervals.

Additional examination techniques were used to access jet behavior. The drag-induced low-pressure region that extends downstream from the nozzle and generates induction was evaluated by inspection of a series of small holes (2.5-mm ID) drilled through the collimating pipe wall. Pressure deviation between the outside air and the collimating pipe interior was indicated by a resultant secondary flow through the small holes. Secondary circulations in the confined annular region between the nozzle and the reattachment plane (fig. 3) were surveyed by observing the induction flow of liquid dyes. These circulations may take the form of toroidal eddies if the velocity ratio between the axial water jet and the annular induction flow is sufficient.

The extent of abrasive mixing within the jet was analyzed through a technique in which efflux flows were made to impinge on the normal surfaces of polished steel plates. The radial distribution of abrasive particles in the jet was interpreted from the pattern of impacts, and the relative magnitude of particle velocities was interpreted from the diameter and depth of impact craters. The steel plate was hard enough to resist alteration due to water impingement, but malleable enough to exhibit plastic deformation craters as the result of particle impaction. A standoff distance of 2.5 cm, measured from the efflux plane of the collimating pipe to the surface of the steel plate, was chosen as representative of field practice. The abrasives used included silica sand, steel shot, glass beads, and carbide grit. Spherical steel shot, which was harder than the steel plate, was used to analyze relative velocity of abrasive particles at impact. Spherical glass beads were used to determine if abrasive particles bounced and reimpacted. The other abrasives (including the steel shot) were used to determine radial distribution.

A predetermined amount of abrasives was manually added to the induction flow almost instantaneously with one pouring motion. The amount of abrasives added was kept small in order to reduce the occurrence of craters that overlapped each other. It was assumed that the mixing behavior of the small measured samples of abrasives and the mixing behavior of a continuous flow are similar, because of comparable jet conditions (albeit, for a short time). The effects of differing abrasive properties (e.g., size and density) were to be considered in analyzing the data.

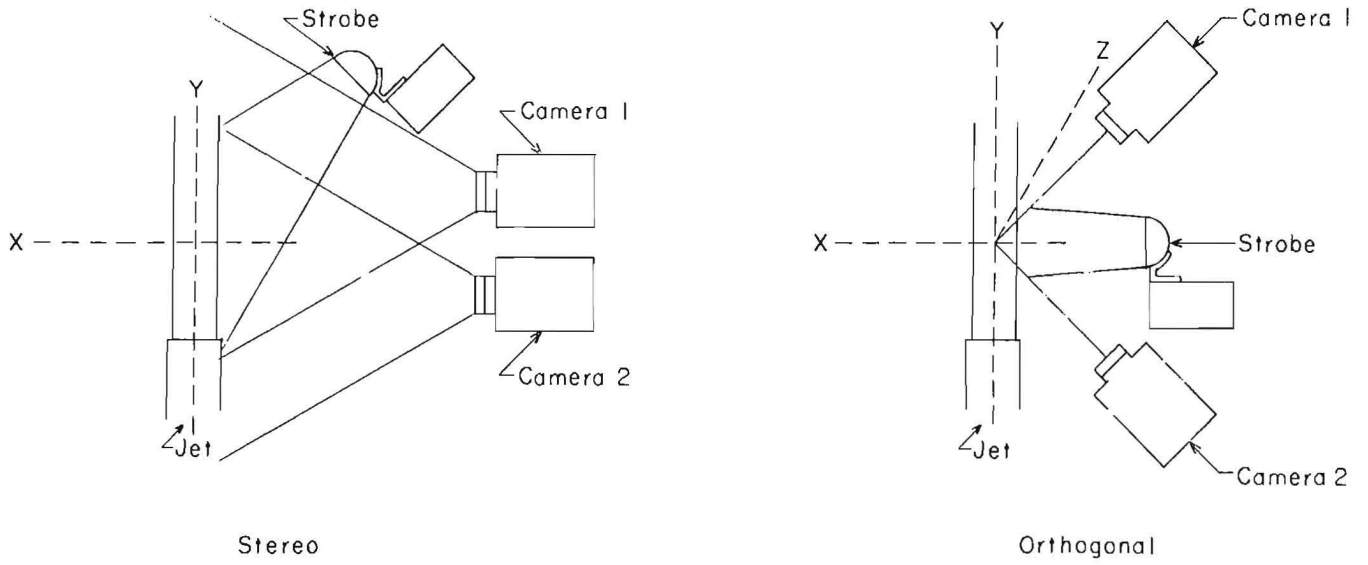


Figure 6.—Two-camera photographic techniques. Left, stereo (jet axis, cameras, and strobe are in X-Y plane); right, orthogonal (cameras and strobe are in X-Z plane, camera views are mutually perpendicular, and jet axis is along Y-axis).

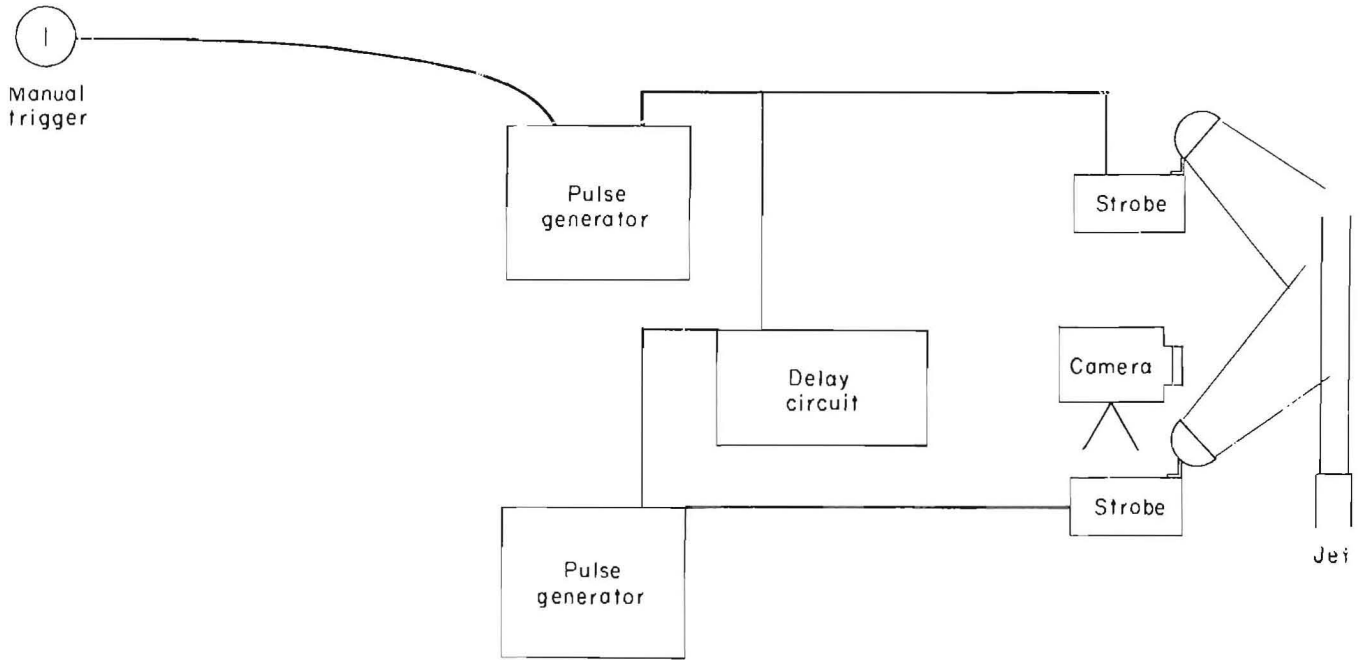


Figure 7.—Multiple-exposure photographic technique.

The distribution of craters within an impact pattern was determined by sectoring the pattern into concentric rings and then determining the relative impact density in each ring. Under a microscope, the center of an impact pattern was oriented with the center of a concentric circle pattern graticule located in the microscope's eyepiece. As a pair of neighboring graticule circles constituted a ring, the number of impacts within each ring was determined. The relative density of impacts within a ring was determined by dividing the number of impacts in a ring by the total number of impacts in the pattern and then dividing this by the area of the ring divided by the area of the pattern. Rings were assigned a representative radius value corresponding to the median radius that bisected the area of the ring.

Crater diameter and depth were determined using a metallographic microscope. Diameters were measured using a scaling graticule in the microscope's eyepiece. Crater depths were determined analytically from the average particle diameter and the crater diameter, after attempts to calculate crater depths from the difference in fine-focus adjustments from the crater rim to bottom proved unproductive because of worn gearing in the microscope.

The operating characteristics of various collimating pipe materials were determined. Flexible tubing was tested to determine functional characteristics. Collimating pipes made of various materials were later tested to evaluate wear response to the passage of abrasives. Wear evaluation included periodic weighing to determine weight loss as a function of time and abrasive throughput and also thickness measurements to determine where the wear was most severe. For thickness measurements, collimating pipes were cut in half along their central axes and the wall thickness was measured with a micrometer.

Alternative collimating pipe designs were tested to determine their influence on jet behavior. The designs included a slotted pipe and one with multiple ports at the efflux end.

An informal experimental design was carried out through a series of single-factor studies to analyze jet response to changes in operating conditions. Initial experiments were conducted to determine the principal elements of behavior underlying the phenomena and to obtain indications of the magnitude of their effects. Detailed study of the phenomena was left to subsequent research. In each single-factor study, a standard combination of factor levels was maintained as the control condition and a single factor was tested at various levels. The independent variables selected for analyses were nozzle

pressure; collimating pipe length and internal diameter, induction port size, number, and location; alignment between the nozzle and the collimating pipe; and collimating pipe material. The relationships between factors were not investigated directly. The standard conditions were as follows: a 69-MPa triplex pump pressure, 61-cm-long collimating pipe, 14-mm-ID collimating pipe, four 6-mm-diameter induction ports drilled into each collimating pipe in a radially symmetric pattern at a distance of 8 mm from the end closest to the nozzle.

Some deviation from the above plan ensued. Flow characteristics with respect to collimating pipe diameter were determined using only 15-cm long collimating pipes. The effect of collimating pipe induction port location was tested using 61-cm-long pipes in an entrainment device designed to permit induction as far as 15 cm from the influx end of the collimating pipe.

The measurements taken during each study made up the values of the dependent variables. The operating characteristics that were measured included reaction forces, induction line pressures, and induction flow rates. Even under assumed steady-state operating conditions, readings from both the high-pressure pump and the reactive force transducer output device were under constant change, although within a narrow range. To assure unbiased measurements, the process of taking these readings was standardized by recording the median readings.

From the operating conditions and measured dependent variables, analytical methods were used to calculate related jet properties. These included flow rates of water and air, and average efflux velocity and power.

Other independent variables were tested for qualitative response: the nozzle alignment with the collimating pipe and the collimating pipe material. For these, responses were observed, not measured.

Flow effects attributable to elements of the transport process (i.e., collimation, mass transfer, and phase effects) were assessed by comparing efflux flow properties of jets with and without those flow elements at various nozzle pressure levels. E.g., the change in jet velocity attributable to induction and collimated transport of abrasives was assessed by comparing the efflux velocity of collimated water jets having air induction with those under similar conditions having induction of both air and abrasives. With free jet flow as a basis, efflux properties of collimated jets without induction, collimated air-water jets, and CAWJ's were evaluated.

EQUIPMENT

The equipment used to generate collimated water-jet flows was similar to that reported in previous Bureau studies (6-8). Figure 8 gives a schematic of the major equipment and its arrangement.

High-pressure water was supplied by a constant-speed triplex pump that controlled working pressures by a control valve and bypass assembly on the pump output line (fig. 9). Triplex pumps, unlike centrifugal pumps, produce pressure pulses with each compression stroke. Such pulses were indicated by the manifold gauge and by vibrations in the high-pressure hose. Configured for 69-MPa working pressure, the pump had a flow rating of 1.35 L/s. This flow exceeded the output of a 2-mm orifice at 69 MPa, and the excess water was routed to a floor drain.

The nozzle design (fig. 10) was similar to that suggested by Nikonov and Shavlovskii for hydraulic monitors

(discussed in reference 16). Features included a 0.23-rad convergence angle and a straight section preceding the orifice that was three times as long as the orifice diameter. This nozzle design is sometimes referred to as a "3-D" type. Through earlier studies (16-17), this design was concluded to be highly efficient for conversion of pressure to kinetic energy when long standoff distances are required. The nozzle was made of AISI Type 304 stainless steel with an orifice diameter of 2 mm.

Dry abrasives were drawn and transported by air, using a commercially available sand induction probe (fig. 11) through 19-mm-ID hose. Connecting the hose to the entrainment apparatus was a 12.5-mm-ID, 10-cm-long, ANSI schedule 40 pipe nipple. At 1.23 cm², this pipe nipple constituted the smallest cross-sectional area in the induction line.

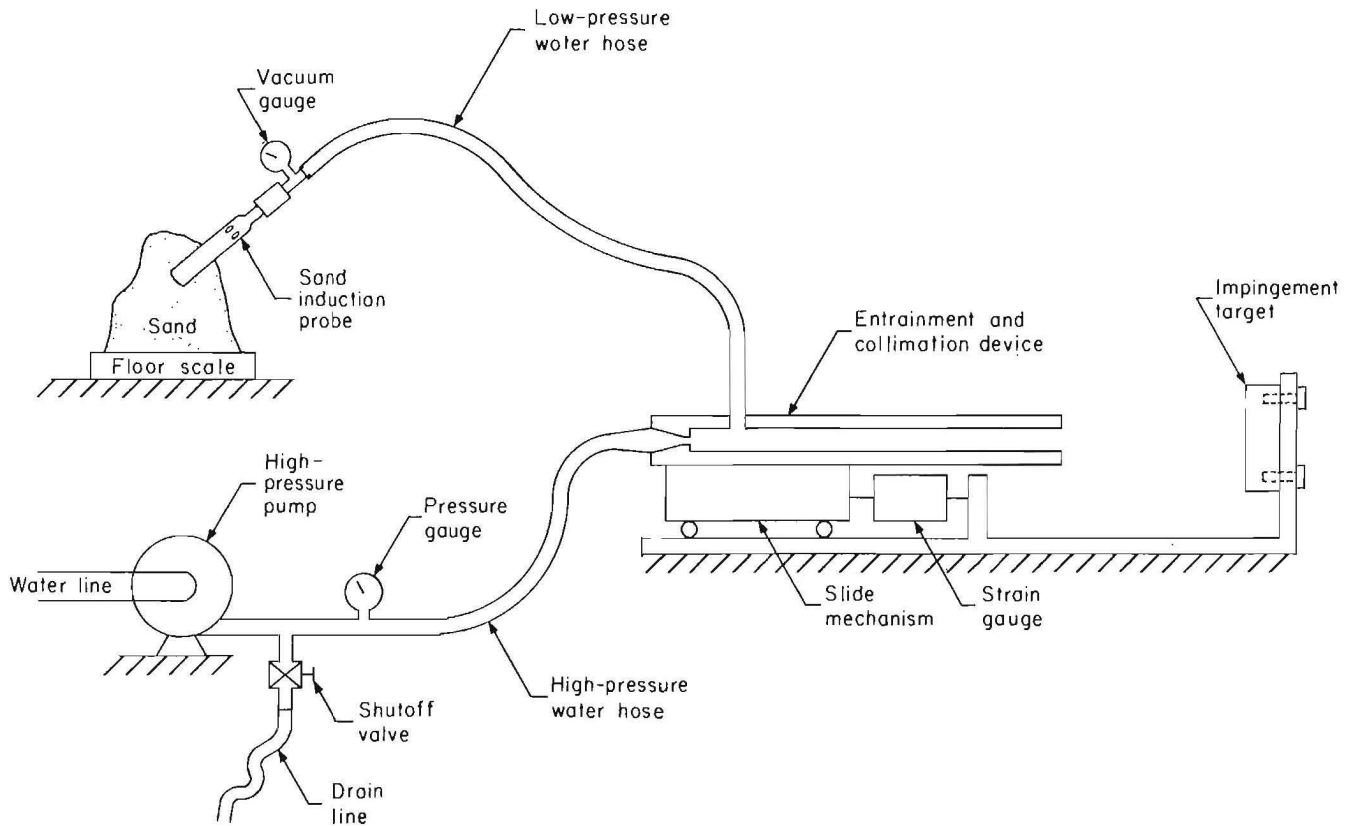


Figure 8.—Schematic of equipment layout.

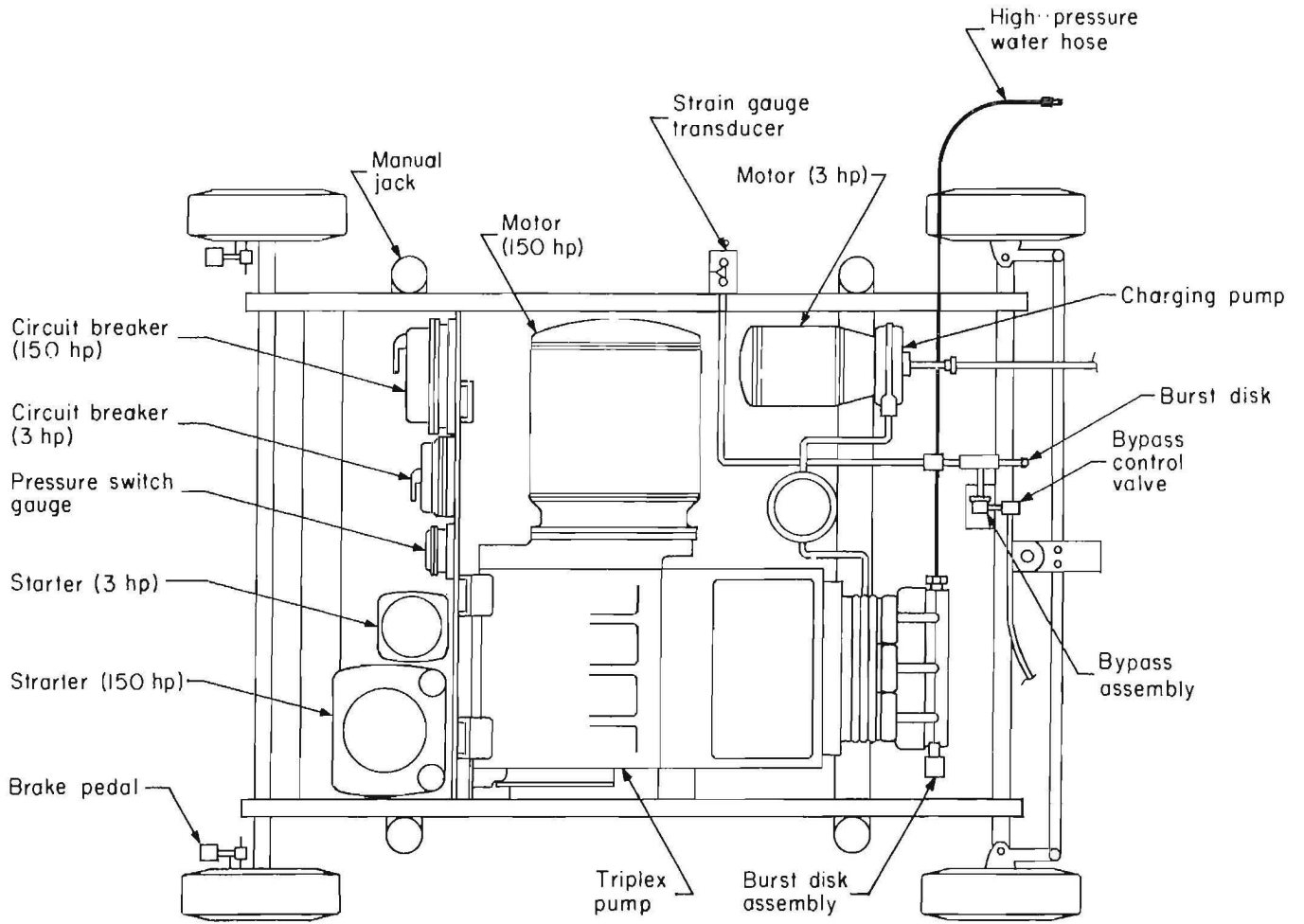


Figure 9.—High-pressure pumping unit.

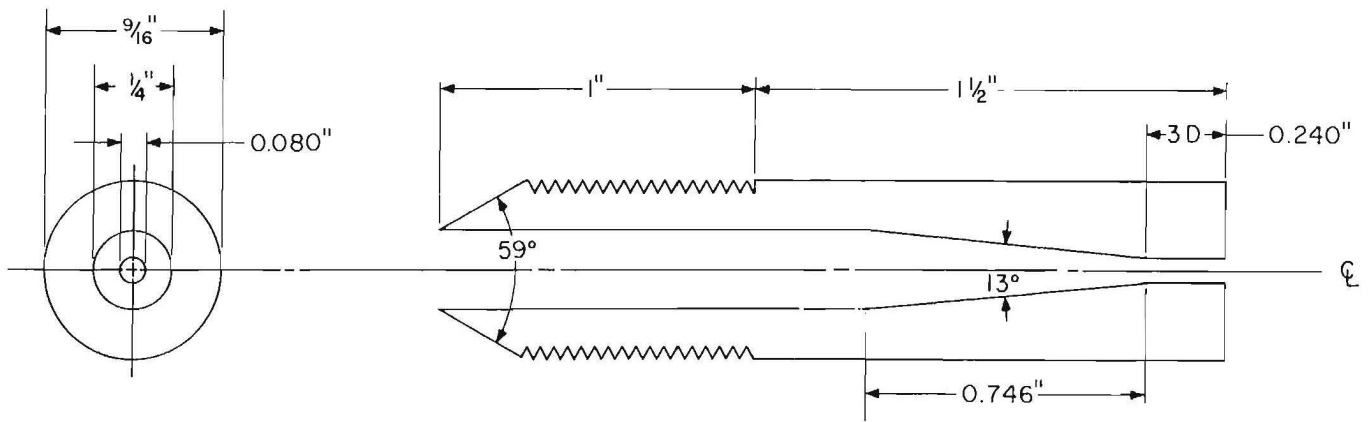


Figure 10.—High-efficiency water-jet nozzle.

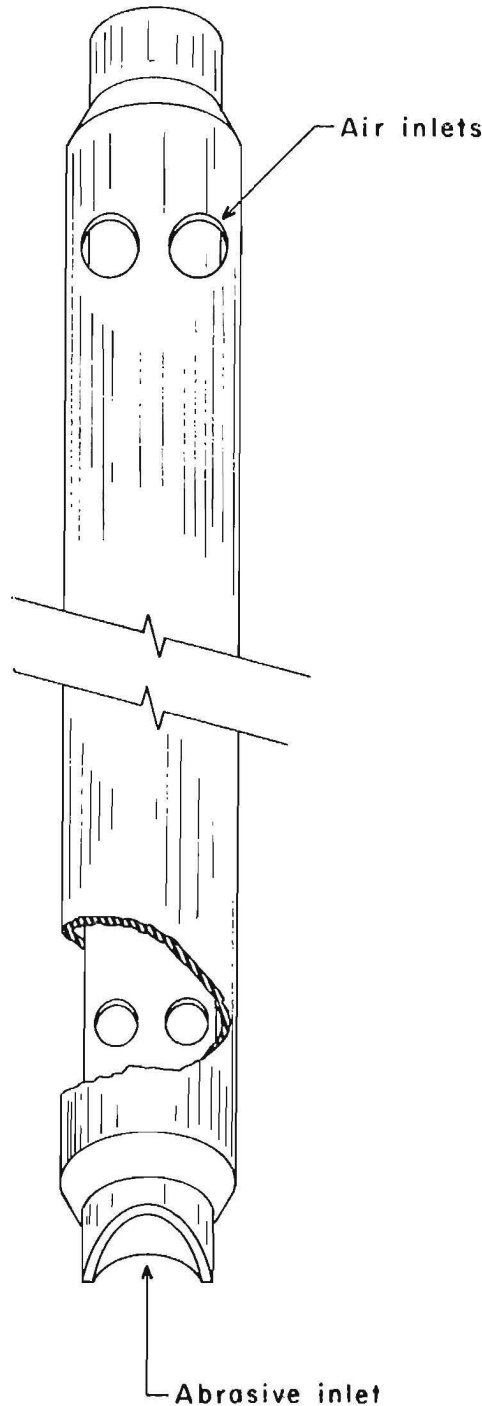


Figure 11.—Abrasive Induction probe.

Different abrasives were used; their properties are listed in table 1. The abrasive used throughout most testing was an angular sand consisting of naturally occurring siliceous aggregate that tested at 88.6 wt pct silicon, with 95 pct of the sand grains falling between 0.99- and 0.83-mm screen sizes. This abrasive had an average grain weight of

1.85 mg and an average particle density of 2.65 g/cm³. Prewashed and bagged, the angular silica sand cost \$0.077/kg. The black copper slag abrasive cost about \$0.12/kg. The black slag abrasive was sometimes used when the jet was photographed, for better contrast of the abrasive against the collimated (aerated) water.

Table 1.—Physical properties of abrasives

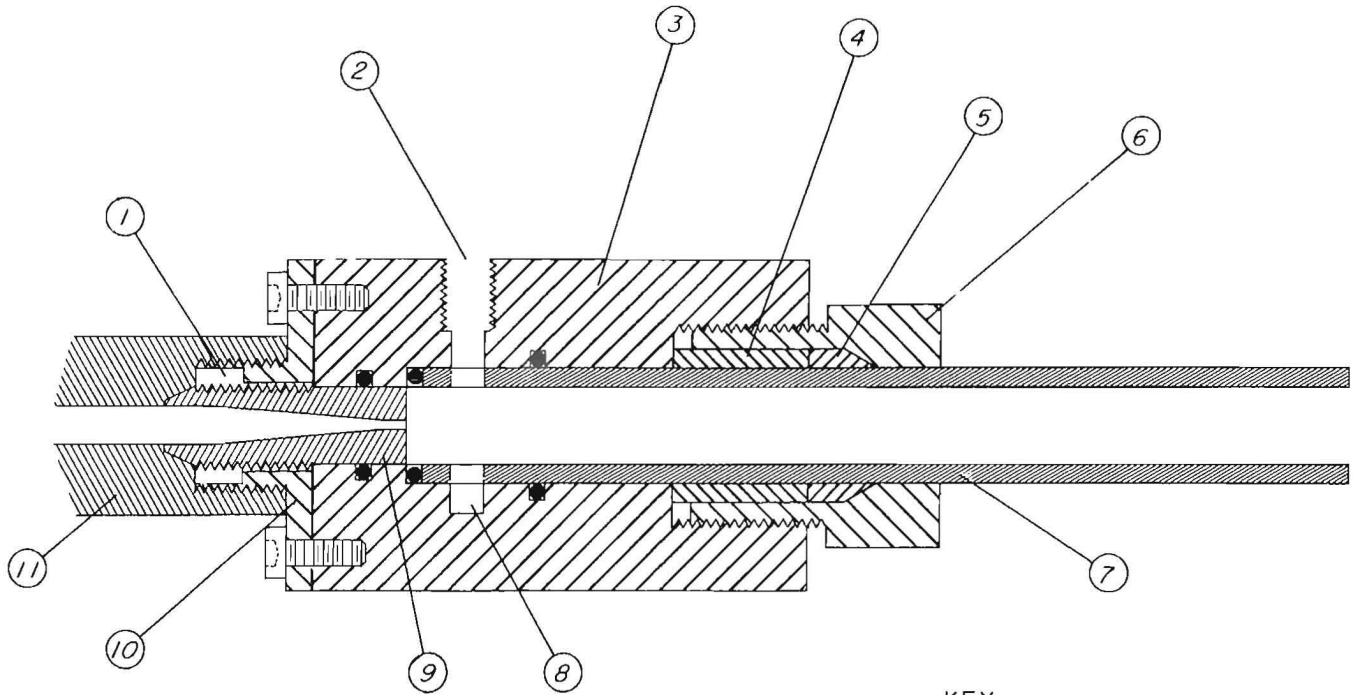
Abrasive	Density, g/cm ³	Median particle diam, mm	Median particle weight, mg	Representative hardness, Rockwell C
Black slag	2.4	0.9	1.3	NAP
Boron carbide grit	2.5	1.0	1.3	NAP
Glass beads	2.5	3.3	43.8	48-50
Silica sand:				
Rounded	2.6	.9	.9	NAP
Angular	2.7	.5	.1	NAP
Steel shot:				
S-230	7.8	.8	2.4	40-48
S-390	7.8	1.3	9.7	40-48

NAP Not applicable.

The steel plates used in impingement trials were 25 mm-thick, hot-rolled ASTM A-36 steel, having an approximate surface hardness of 10 Rockwell C, ground to a 2.5- μ m surface finish, with countersunk holes in each corner for nonobtrusive mounting. The spherical abrasives used in these trials included steel shot and glass beads (table 1). Two sizes of steel shot were used, size Nos. S-230 and S-390 according to SAE J444 standard size specifications for cast shot. The S-230 steel shot was more spherical and regular in size and was used when crater depth and diameter were analyzed. Both sizes of steel shot had an approximate hardness of 44 Rockwell C. Samples of S-230 steel shot averaged 0.78 mm in diameter and 2.4 mg in weight, and the S-390 steel shot averaged 1.3 mm in diameter and 9.7 mg in weight. The glass beads were laboratory boiling beads averaging 3.3 mm in diameter and 44 mg in weight. Rounded silica sand, steel shot, glass beads, and carbide grit were used to determine particle impact distributions.

The three-phase constituents (i.e., water, air, and abrasives) were brought together in an entrainment apparatus (fig. 12) that was later modified to allow greater flexibility in experimental design (fig. 13). This apparatus was mounted to a test stand with a parallel-arm slide mechanism that transferred reactive forces to a connected force transducer.

Most collimating pipes were half-inch-nominal-ID ANSI schedule 80 conduit, ASTM A53/A120 seamless carbon steel pipe with a lacquer coating over a pickled finish, having an inside diameter of 1.387 cm and a wall thickness of 3.73 mm. These pipes cost \$3.74/m and have an allowable working pressure of 25.4 MPa at 232° C. Collimating pipes were cut to the desired lengths and turned down on a lathe to remove the nonmetallic finish and provide a better fit with the seals in the entrainment apparatus. An O-ring was compressed between the collimating pipe and the high-pressure nozzle to form a seal. Holes were



KEY

- | | |
|---------------------------------------|----------------------|
| 1 Collar nut | 6 Gland nut |
| 2 3/8-in NPT female pipe thread | 7 Collimating pipe |
| 3 3-in steel round bored and machined | 8 3/8-in groove |
| 4 Collar | 9 3-D nozzle |
| 5 Slotted collet | 10 Gland nut |
| | 11 Straight coupling |

Figure 12.—Experimental entrainment apparatus.

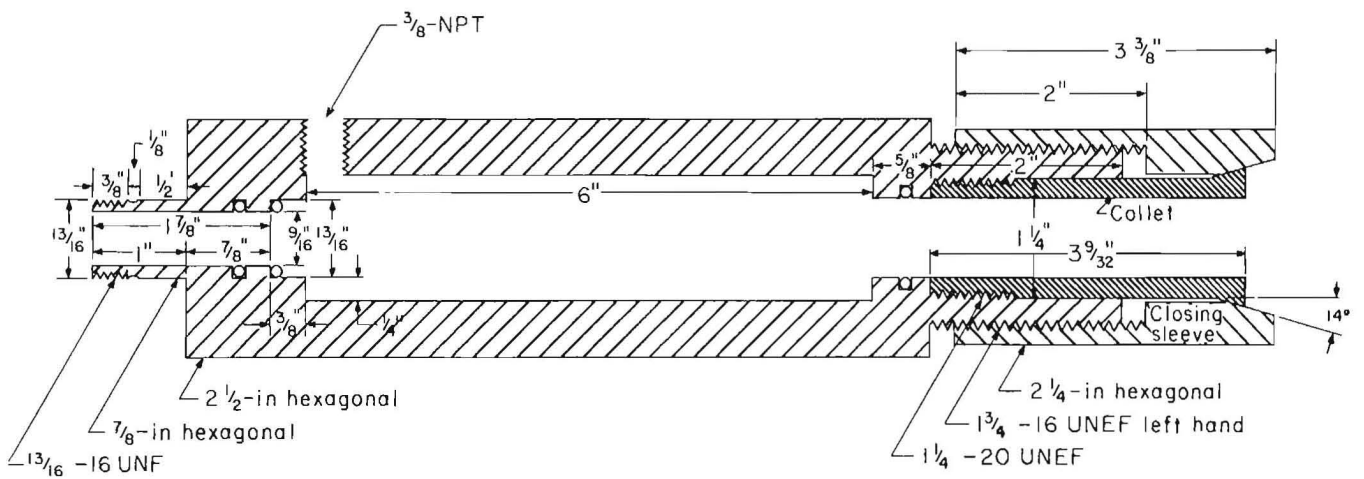


Figure 13.—Modified experimental entrainment apparatus.

drilled into the collimating pipes to permit induction. Collimating pipes exceeding 1.5 m in length were supported on rollers to prevent bending under their own weight; shorter pipes were suspended in a cantilevered manner.

The other collimating pipe materials included polyvinyl, polyurethane, and tungsten carbide tubing. The polyvinyl was a 13-mm-ID flexible tubing with 1.6-mm wall thickness. The polyurethane tubing was vacuum rated with 13-mm ID and 1.6-mm wall thickness. Tungsten carbide pipe [used with the Bureau's AWJ drill (8)] was also 13-mm ID, with a cost of about \$945/m.

The alternative collimating pipe designs included a slotted pipe, a pipe with thicker walls, and one with multiple ports at the efflux end. The slotted pipe was a 60-cm-long, half-inch-nominal-ID ANSI schedule 80 pipe with a single 2.5-mm-wide slot that extended 45 cm from the efflux end. The pipe with thicker walls was ANSI schedule 160 half-inch-nominal seamless black pipe, with a 4.75-mm wall thickness, costing about \$6.81/m. The ventilated pipe was a 60-cm-long, half-inch-nominal-ID ANSI schedule 80 collimating pipe with thirty 2.5-mm-ID holes, angled at 0.8 rad downstream inward in the final 15-cm of the pipe. The pattern of holes was dispersed to prevent adjacent holes from having an aggregated effect.

As operating pressures increased, the tendency of the high-pressure water hose to straighten was a potential source of error in the reactive force measurements. To reduce the effect of the water hose forces on the test stand, a 1.57-rad pipe elbow was plumbed between the hose and the entrainment apparatus.

Sections of joined 3-m-long, 7.6-cm-ID pipe were axially aligned with the water-jet efflux at a downstream standoff distance of 10 cm so that the spray of water and abrasives would be confined and not inconvenience other laboratory activities. These sections normally totaled 12 m in length and required an enclosure to confine the spray and a splash plate to prevent damage to the enclosure.

The equipment used to photograph the jet included 35-mm cameras, lenses, tripods, stroboscopes, electronic pulse generators, polarizing screens, ultraviolet lens filters, an autowinder, and 1000-ASA color film. One of the pulse generators was equipped with a variable-delay circuit that was controllable between 0.1 μ s and 1.0 s. Two strobes were used with the delay circuit. The polarizing screens were circular polarizers with 1/4-wave rotation. The usual lens configuration was a 20- to 135-mm short telephoto-zoom lens in combination with a 4.0-cm focal-length closeup filter.

Abrasive consumption was assessed by monitoring the weight change of the stockpile on a digital platform scale. The slide mechanism that held the entrainment and collimation device transferred reaction forces (thrust) to a connected force transducer.

ANALYTICAL METHODS

Analytical equations were used to calculate unknown values from measured data.

Since water pressure readings were taken at the pump, nozzle pressures were estimated from measured pump pressures and calculated flow losses between the pump and nozzle. The pressure (p) corresponding to flow losses attributable to the high-pressure hose and fittings between the pump and the nozzle was estimated using a metric conversion of the Hazen-Williams head-loss formula (10),

$$\Delta p = \frac{(31.1921)(L/0.3048)(Q \cdot 15.85077)^{1.85}}{[(C)^{1.85}(D_h/2.54)^{4.8655}]}, \quad (1)$$

where Δp = pressure loss, kPa,

L = length, m,

Q = flow rate, L/s

C = Hazen-Williams constant,

and D_h = hose inside diameter, cm.

In equation 1, length was the sum of actual hose length (7.62 m) and equivalent lengths for fittings (2.13 m). The Hazen-Williams constant was taken as 140 to correspond to the plastic core of the high-pressure hose. The hose inside diameter was 1.27 cm.

Air density was calculated from temperature, pressure, and humidity data, using the method presented in table 2.

For calculations involving material balance (mass input equals output), it was assumed that the experimental batch flows (once initiated) were continuous and steady state and that volumetric flow rate (Q) at a given location equals flow velocity (v) times cross-sectional area (A):

$$Q = vA. \quad (2)$$

It was assumed that the volumetric flow rates of water and abrasives were continuous throughout the collimated flow and that air made up the remaining volume. Assuming flow continuity, the composition of a collimated water jet by mass was determined from the mass influx rates of water, air, and abrasives. It was assumed that the mass flow rate of water for a given nozzle pressure was unaffected by the operating configuration, whether free jet or collimated. In describing flow constituent percentages, water was assumed to remain in a liquid phase with a density of 1.0 g/cm³ throughout.

TABLE 2.—Air density calculations

Line vacuum pressure, ¹ kPa	Line vacuum pressure, ² mm Hg	Air density, ³ g/L	Line vacuum pressure, ¹ kPa	Line vacuum pressure, ² mm Hg	Air density, ³ g/L
0.0	0.0	1.189	10.0	75.0	1.067
0.5	3.8	1.183	10.5	78.8	1.060
1.0	7.5	1.177	11.0	82.5	1.054
1.5	11.3	1.170	11.5	86.3	1.048
2.0	15.0	1.164	12.0	90.0	1.042
2.5	18.8	1.158	12.5	93.8	1.036
3.0	22.5	1.152	13.0	97.5	1.030
3.5	26.3	1.146	13.5	101.3	1.024
4.0	30.0	1.140	14.0	105.0	1.018
4.5	33.8	1.134	14.5	108.8	1.016
5.0	37.5	1.128	15.0	112.5	1.005
5.5	41.3	1.122	15.5	116.3	.999
6.0	45.0	1.115	16.0	120.0	.993
6.5	48.8	1.109	16.5	123.8	.987
7.0	52.5	1.103	17.0	127.5	.981
7.5	56.3	1.097	17.5	131.3	.975
8.0	60.0	1.091	18.0	135.0	.969
8.5	63.8	1.085	18.5	138.8	.963
9.0	67.5	1.079	19.0	142.5	.957
9.5	71.3	1.072	19.5	146.3	.950
10.0	75.0	1.067	20.0	150.0	.944

¹Chosen at regular intervals.²Unit conversion from first column.³Calculated from following equation using ambient conditions shown:

$$\rho = 1.2929 \cdot (273.13/T) \cdot \{(B - b) - 0.3783e\}/760\}$$

where ρ = air density, g/L,

T = temperature; ambient = 285.15 K (12° C),

B = barometric pressure; ambient = 732 mm Hg (at 313-m altitude),

b = induction line vacuum pressure, mm Hg,

and e = vapor pressure; ambient = 6.54 mm Hg (dew point of 5° C).

Source: Weast (18)

For air induction without abrasives, anemometer velocity readings multiplied by flow area (i.e., induction line internal area minus the profile area of the anemometer wand) were used to determine volumetric flow rate by equation 2. The volumetric flow rate multiplied by the density (ρ) gives the mass flow rate.

$$\delta M/\delta t = \rho Q, \quad (3)$$

where M = mass

and t = time.

The mass flow rate of air was calculated from the calculated volumetric flow rate and the estimated air density, using equation 3.

Using orifice pressure as the basis, efflux velocity, reactive force, and mass flow can be calculated from the fluid density and the area of the orifice. A flow can be treated as steady and incompressible for pressures and speeds that are not too high, even though the fluid is compressible and the flow is turbulent (19). Compressible

airflow can be treated as incompressible for a pressure drop of less than 10 pct (20). Treating the flow as incompressible, the mass flow in time δt is

$$\delta M = \rho A v \delta t. \quad (4)$$

In the case of discharge flows from nozzles, equation 4 is especially useful in calculating average efflux velocity from reactive force and nozzle orifice size, since errors inherent to determining the nozzle's actual orifice pressure and velocity coefficient are avoided.

The rate at which momentum is transferred out of a system can be interpreted as the force exerted on the system by the exiting mass. Momentum rate equals reactive force. From Newton's second law for systems of variable mass, the reactive force (F) is

$$F = v(\delta M/\delta t). \quad (5)$$

Nozzle efflux mass flow rates were estimated, using equation 5 from the measured reaction forces and the estimated efflux velocities.

For collimated flows, collimating pipe efflux velocities were calculated, using equation 5, by dividing measured reaction forces by calculated total mass flow rates. Total mass flow rates were determined by adding the component mass flow rates (i.e., air, water, and abrasives). Flow rates determined from free jet tests were used as the waterflow rates for given nozzle pressures under collimated conditions.

Substituting for δM in equation 5 with the equality from equation 3, the reactive force can be rewritten as

$$F = \rho A v^2. \quad (6)$$

Equation 6 was used to calculate nozzle efflux velocities, since nozzle orifice size could be more accurately measured than the discharge rate.

Using a derivation of Bernoulli's equation that assumes negligible fluid velocity upstream of the nozzle in comparison with the nozzle efflux velocity (19), velocity of flow across a pressure gradient is

$$v = (2\Delta p / \rho)^{0.5}, \quad (7)$$

where Δp = gauge pressure.

For practical purposes, the idealized velocity given by equation 7 should be reduced by a velocity coefficient that is characteristic of the nozzle. For water-jet nozzles, a velocity coefficient of 0.97 is generally used.

Substituting for velocity in equation 6 by the equality given in equation 7, reactive force becomes

$$F = 2A\Delta p. \quad (8)$$

By equating the nonvelocity terms of equations 4 and 7 and then rearranging, the mass flow rate becomes

$$\delta M / \delta t = (2A^2 \rho \Delta p)^{0.5}. \quad (9)$$

For nozzle flows, equation 9 is usually modified by a discharge coefficient of 0.7 to 0.9.

In two-phase flow (e.g., phase a and phase b), the overall density and mass flow rate correlate to the constituent volumetric flow rates and densities of each phase by the following relations:

$$\rho_{(a+b)} = \{(Q_a \rho_a) + (Q_b \rho_b)\} / (Q_a + Q_b); \quad (10)$$

$$\delta M_{(a+b)} / \delta t = (Q_a \rho_a) + (Q_b \rho_b). \quad (11)$$

Substituting component density and volumetric flow rate factors into equation 9 and transforming, the volumetric flow rate of one constituent becomes

$$Q_a = \{(8A^2 \Delta p \rho_a + [Q_b(\rho_a - \rho_b)]^2)^{0.5} - Q_b(\rho_a + \rho_b)\} / 2\rho_a. \quad (12)$$

Induction line airflow rates with both air and abrasive influx were estimated using equation 12. In this calculation, gauge air pressure readings, the area of the induction line near the gauge (1.23 cm²), air density calculations based on pressure (table 2), and the density and flow rate of abrasives were used.

Bernoulli's equation can be used to calculate the power available in a fluid stream by multiplying the total energy per unit mass by the mass flow rate (10). Neglecting pressure and gravitational head, power (P) equals kinetic energy per unit mass times the mass flow rate, which can be written as

$$P = 0.5(\delta M / \delta t)v^2. \quad (13)$$

By equation 5, reactive force can be substituted for $(\delta M / \delta t)v$ in equation 13 to give

$$P = 0.5Fv \quad (14)$$

Efflux power as given in the results section and in the tables was determined, using equation 14 from estimated efflux velocities and measured reactive forces.

For impacts in malleable steel from spherical particles, estimates of particle impact conditions were made using indentation data and analytical solutions to stress-strain behavior. When a hard sphere is pressed into a ductile material, the restraint of the surrounding nondeformed ductile material channels most of the applied load into hydrostatic compressive stress (21). If no fracture or larger scale deformation occurs, the load reaches a constant value or maximum load. This maximum load is approximately three times the tensile strength of a ductile material, or more if strain hardening occurs (21). Abrasive particle impact force and velocity may be determined from particle impact craters and the deformation behavior of the impacted material. As hardness scales relate applied load to the contact area of a nondeforming indenter, material yield strength relates the force applied by an indenter to the size of the indentation. The Meyer ball hardness equation is

$$M_B = 4F / \pi D_c^2 \quad (15)$$

where F = applied load,

and D_c = impression (crater) diameter.

This equation relates the hardness value to the projected area of a spherical indenter and gives a good approximation of the average plastic flow stress (pressure) because the radial forces on the crater sidewalls counteract each other (21). For nonstrain hardening materials, the equation

$$M_B \approx 3.2Y, \quad (16)$$

where Y = yield strength of the ductile material,

is valid for a variety of materials including mild steels when the ratio of impression diameter to indenter diameter is near 0.4 (21).

Assuming a spherical impression, crater depth can be estimated from the diameters of the spherical indenter and the crater:

$$d = D_i/2 - [(D_i/2) \cos (\sin D_c/D_i)] \quad (17)$$

where d = crater depth,

and D_i = diameter of a spherical indenter.

RESULTS

GENERAL BEHAVIOR

A pressure drop due to line friction (equivalent length additions were used to compensate for fittings) was calculated as 617 kPa for an operating pressure of 69 MPa. This loss was small in comparison with the pump output pressure (about 0.9 pct), but this difference was inherent to all tests.

The spatial density of abrasive particles in the collimated jet efflux was estimated for a 69-MPa operating pressure. Using silica abrasive with a representative 130-g/s abrasive flow rate and 1.85-mg average particle weight, dividing mass per time by mass per particle yields about 70,000 particles per second traveling through the collimating pipe. At an efflux velocity of 284 m/s, the spatial density for particles in the jet efflux would be about 1.6 per cubic centimeter. With this spacing, it seems unlikely that interaction between particles would be great.

Visual Form of Jet

Examination under stroboscopic lighting of 1 to 417 flashes per second and by high-speed photography found no indication of pulsed jet flow in flows exiting the nozzle or collimating pipe. This indicated that the line pulsations noted in the high-pressure hose did not transcend the nozzle.

The water jet was photographically shown to expand after exiting the nozzle orifice as a free jet confined within a collimating pipe (fig. 14). Without abrasives, the included angle of the water-jet expansion was about 0.08 rad as the expanding axial waterflow reattached to the collimating pipe about 14 cm downstream of the nozzle efflux plane in a 1.27-cm-ID transparent tube. Downstream from the point of reattachment, the nonabrasive flow constituents were seen to fill the collimating pipe as a nearly homogeneous mixture (fig. 15). The collimated water jet resembled a dense suspension of fine water particles in air. Photographs were unable to resolve individual water droplets because of their small size and high velocity.

Photographs of collimated efflux flows (fig. 16) show an aerosol mixture of air and water with the visible abrasive particles widely dispersed. Abrasive particles near the jet axis were obscured by the high reflectivity and light dispersion of the water jet. Because the center of the jet is hidden, orthogonal and stereo photographs were not useful in analyzing the jet interior.

Examined photographically, the jet exiting a 60-cm-long collimating pipe was shown to transform from a nearly coherent stream to an atomized and collimated flow with increasing nozzle pressure. At pressures below 0.35 MPa, the jet showed no signs of reattachment within the collimating pipe or entrainment of air. At nozzle pressures of about 3.5 MPa, photographs of efflux flows showed a strikingly nonhomogeneous water spray containing discernable droplets and no axial core of water. For nozzle pressures approaching 69 MPa, water droplets in the efflux flow were too small and too evenly dispersed for individual droplets or the spacing between adjacent droplets to be distinguished.

In collimated efflux flows with no induction, it was evident from photographs and from the efflux velocities that water did not coherently fill the collimating pipe, even with collimating pipes as long as 6 m. With cross-sectional areas of 3.14 mm² for the nozzle orifice and 151 mm² for the collimating pipe, jet velocity would have to drop by almost a factor of 50 for the water jet to coherently fill the collimating pipe. The resultant drop in momentum and kinetic energy would be 98 and 99.96 pct, respectively.

Multiple-exposure photographs of collimated abrasive efflux jets (fig. 16D) indicated that abrasive particles in the jet's exterior travel along streamlines that are oriented in an axial flow direction. Particle velocities determined from photographs ranged from 200 to 300 m/s for 69-MPa nozzle pressures.

From examination of photographs, some efflux abrasive particles appear smaller than the size range that entered the induction line. This implies that some abrasive particles are broken prior to leaving the collimating pipe. Fracturing of abrasive particles would most likely occur along areas of the collimating pipe and induction equipment that later show wear. Actual size distributions of efflux abrasive particles were not determined because of difficulties in particle collection.

The efflux flow of the CAWJ was observed to give a faint pink colored glow that diminished in intensity with downstream distance from a steel collimating pipe. This illumination was observable in a darkened room, but was difficult to photograph. Heat streaking from abrasive collisions with the steel collimating pipe's interior surface is the most likely cause.

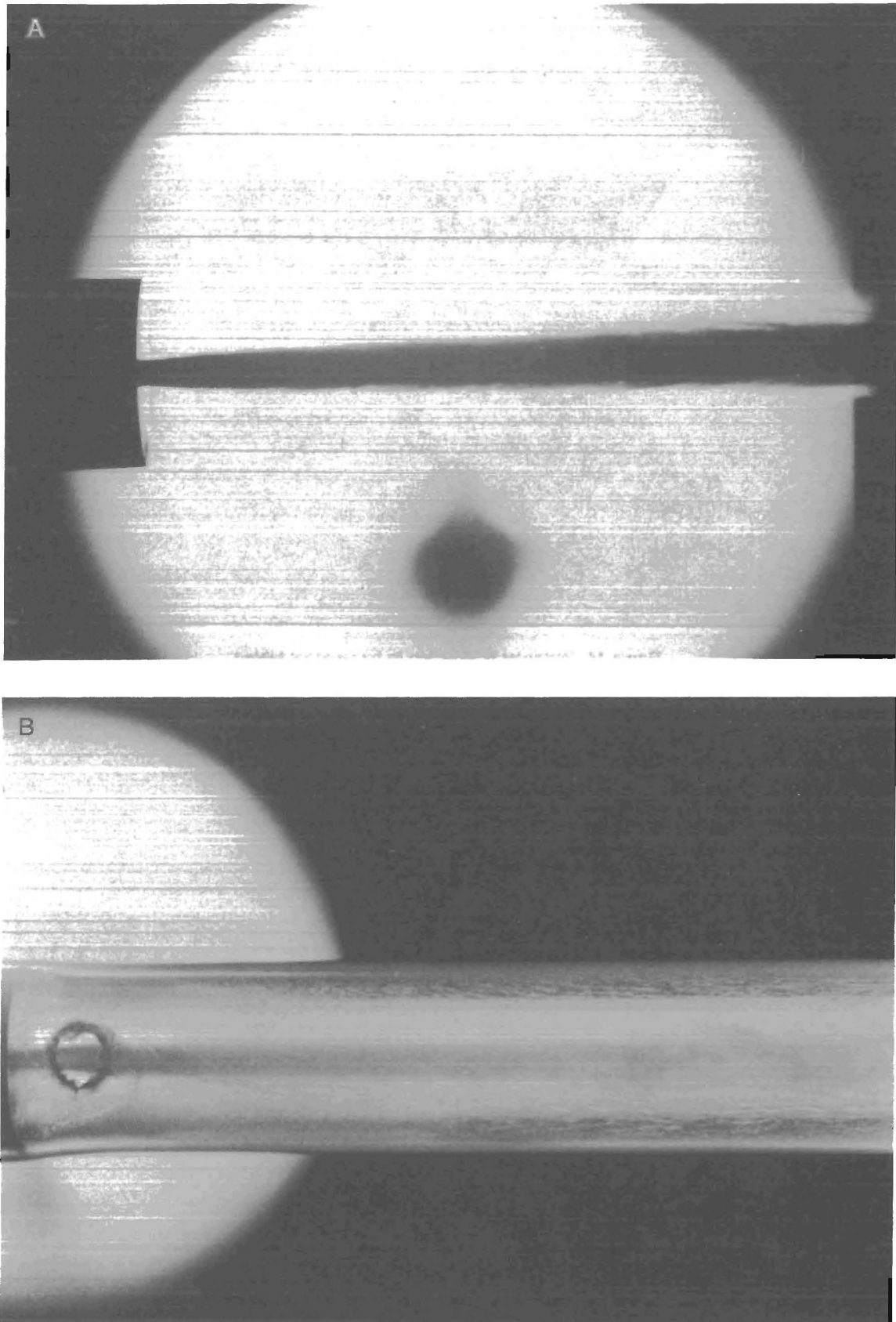


Figure 14.—Water-jet expansion. A, In open air; B, into a transparent ported collimating pipe.

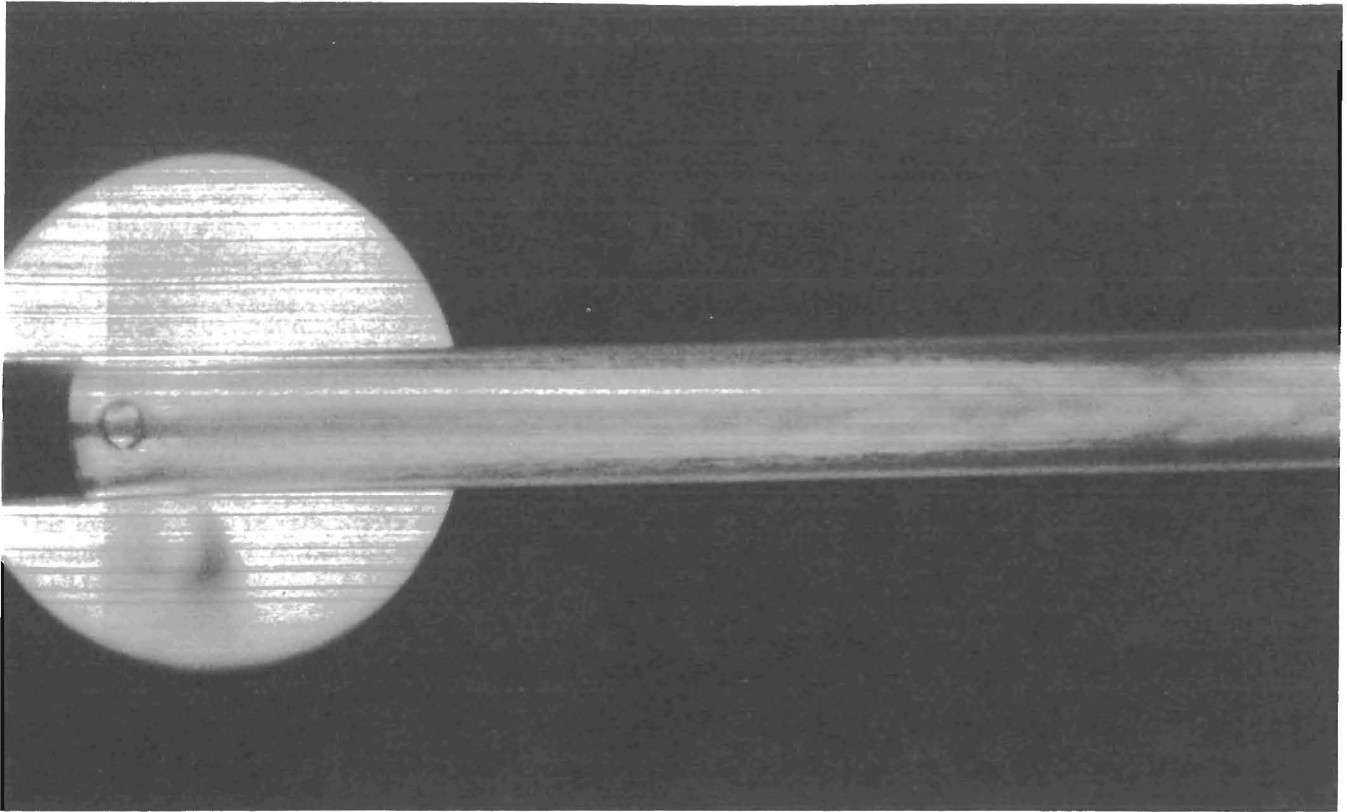


Figure 15.-Water-jet collimation in transparent tubing.

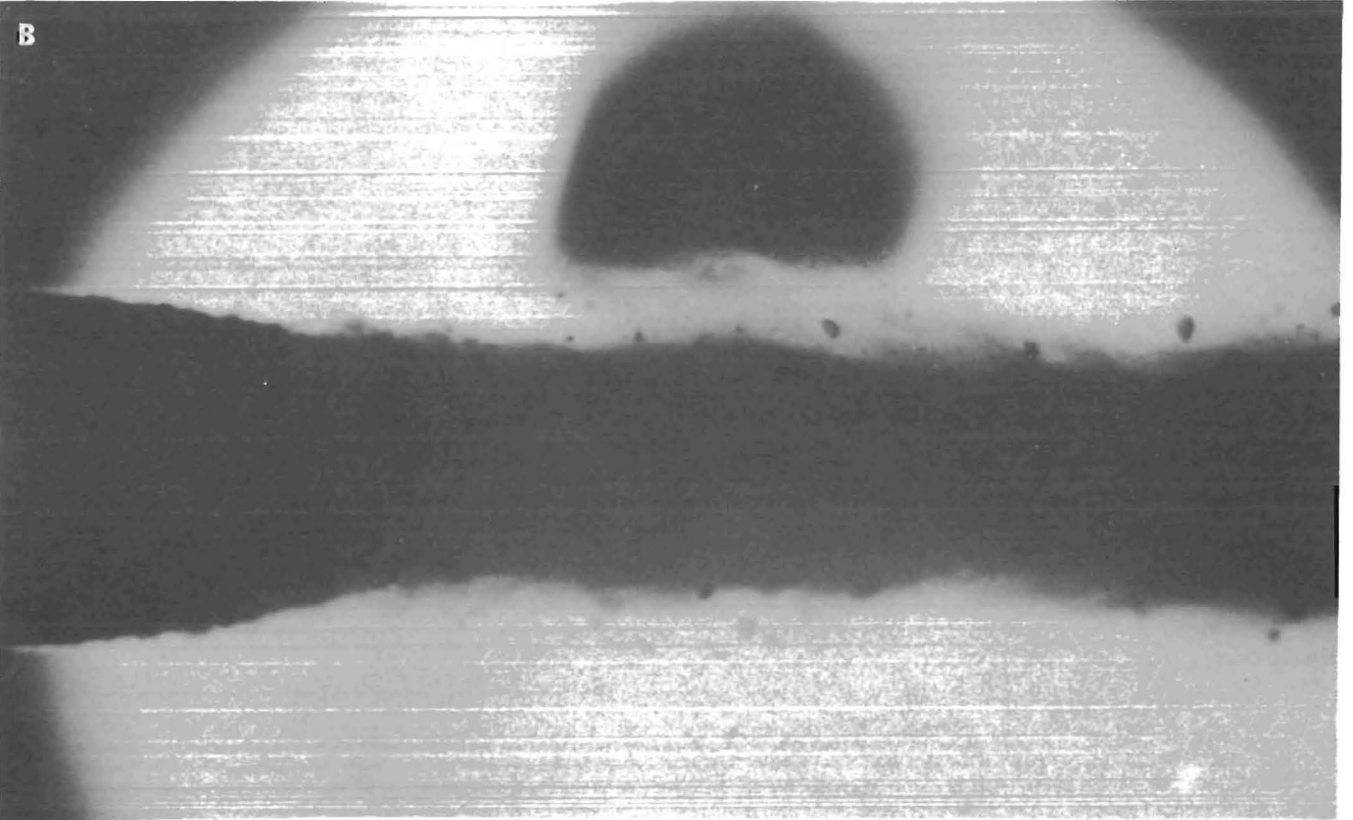
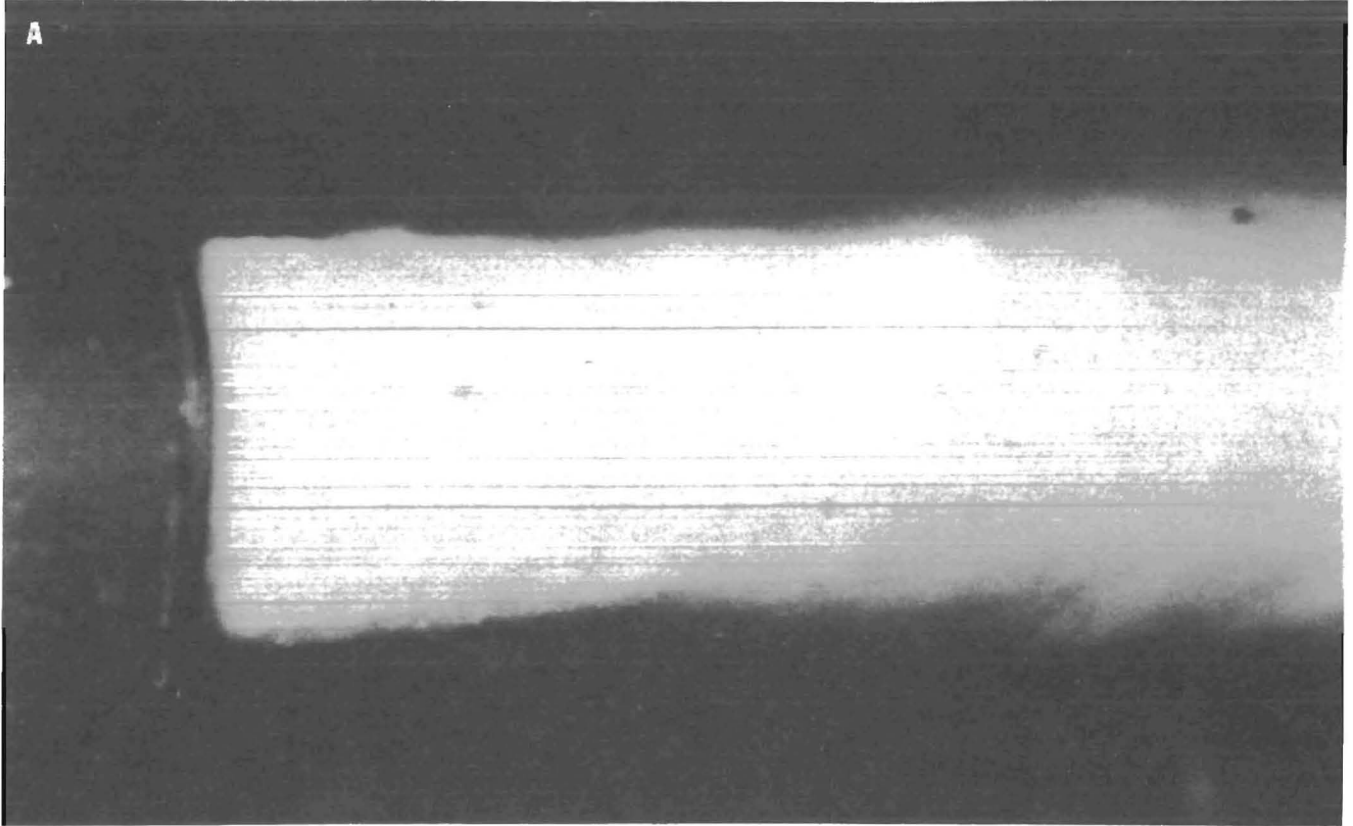


Figure 16.-Collimated abrasive water jet. A, Diffused frontal lighting; B, diffused backlighting.

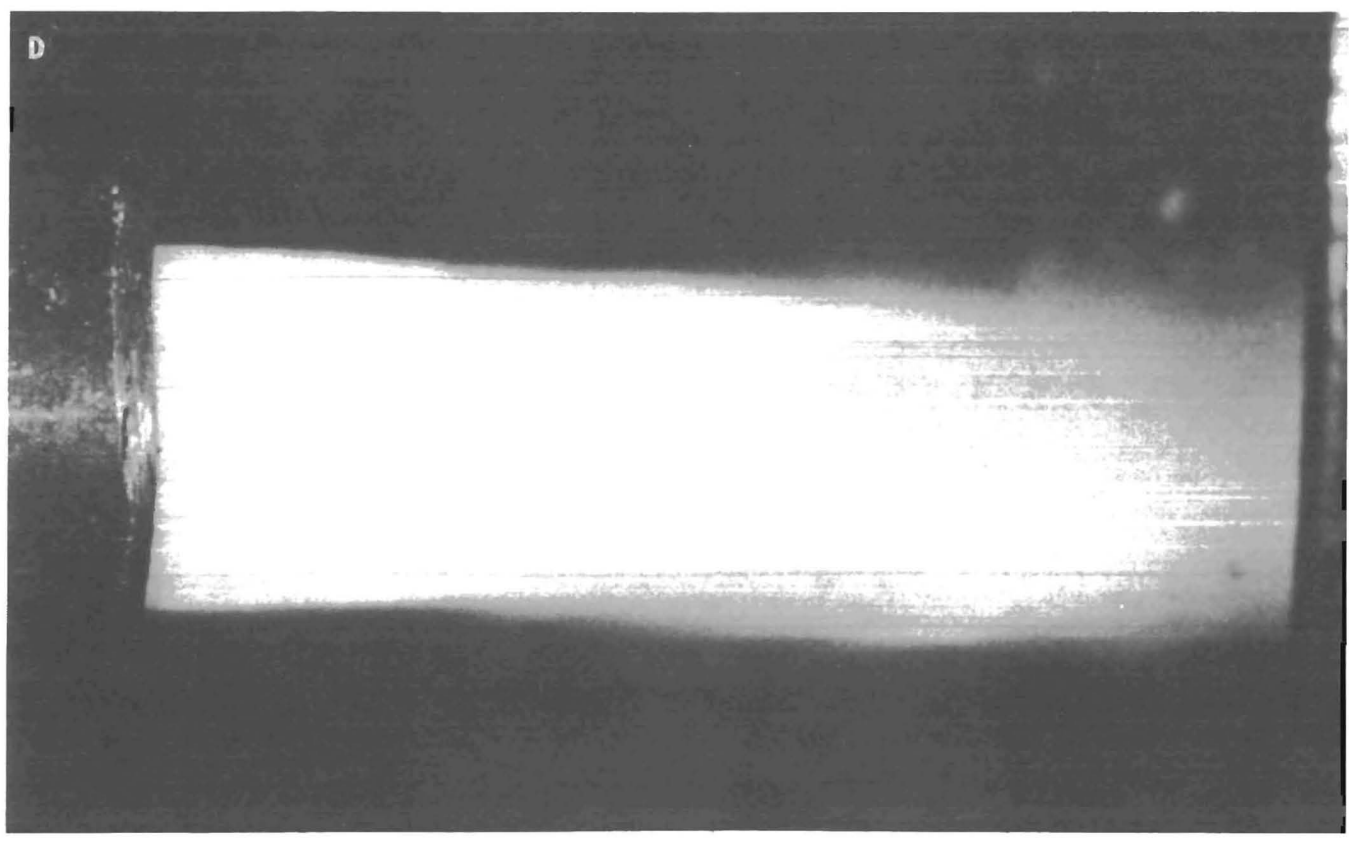
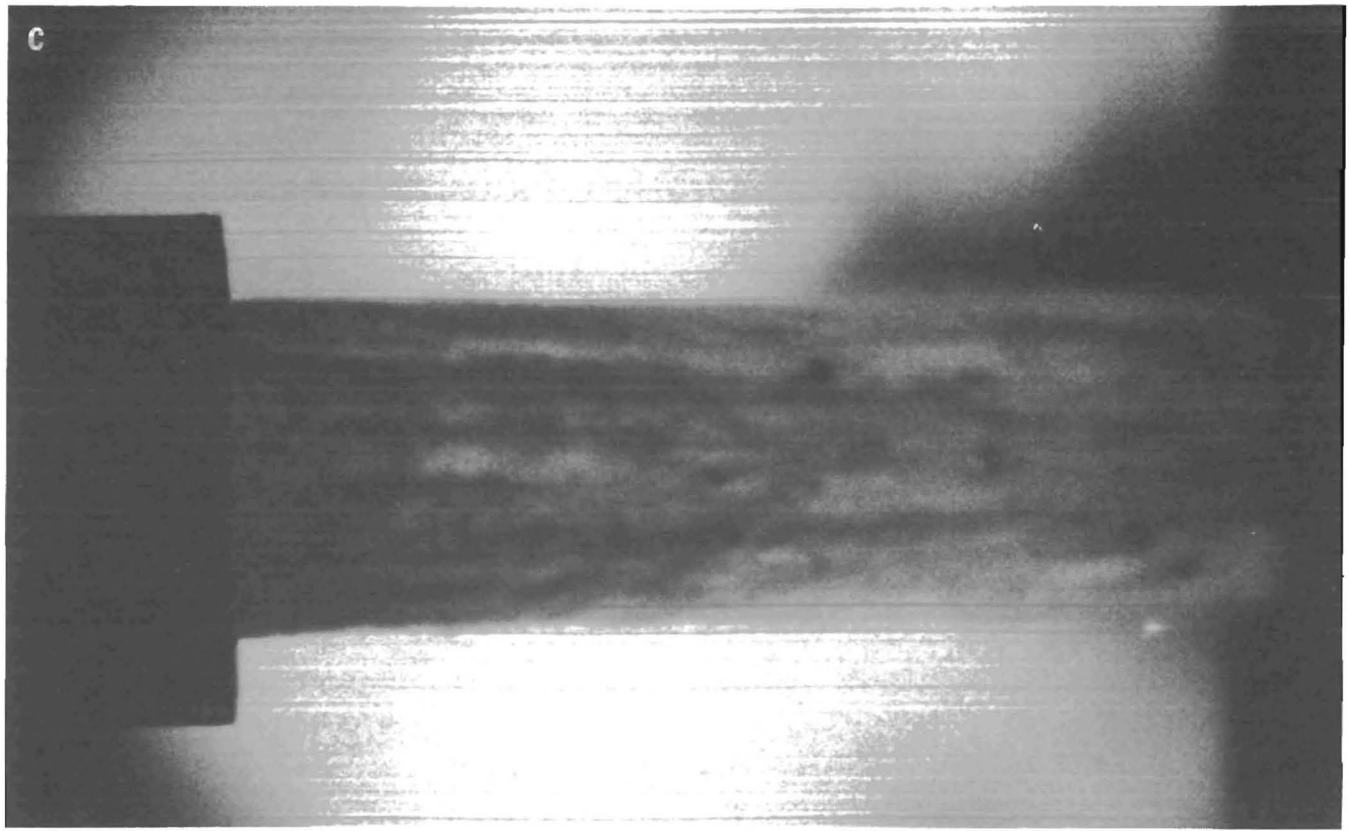


Figure 16.-Collimated abrasive water jet-Continued. C, Polariscopic backlighting; D, double exposure.

Circulation Zones Within Collimating Pipe

A circulation zone between the induction ports and the nozzle was viewed through transparent collimating pipes. As described by others (12, 22-24), this circulation is typical of those caused by viscous interaction of adjacent flows. Liquid dye, injected by syringe near the induction ports, traveled toward the nozzle along the inside surfaces of polyurethane tubing. When glass tubing was used for abrasive flows, the presence of abrasive particles between the induction ports and the nozzle also gave evidence of a circulating flow (fig. 17).

While the collimated water jet was operated without abrasives, ice was observed on the interior walls of

transparent collimating pipes between the induction ports and the nozzle. Relative humidity in the laboratory was high, and there was much condensation on cold metal plumbing. The ice was apparently produced as moisture-saturated air encountered the low-pressure region near the nozzle in polyurethane tubing. Ice formation was not observed during tests using steel collimating pipes because the pipes were opaque. Because high thermal conductivity inhibits the localization of cold spots, it is questionable whether ice would form in steel collimating pipes or remain solid long after a test was completed. Ice formation indicated that the material transfer process was not isothermal.

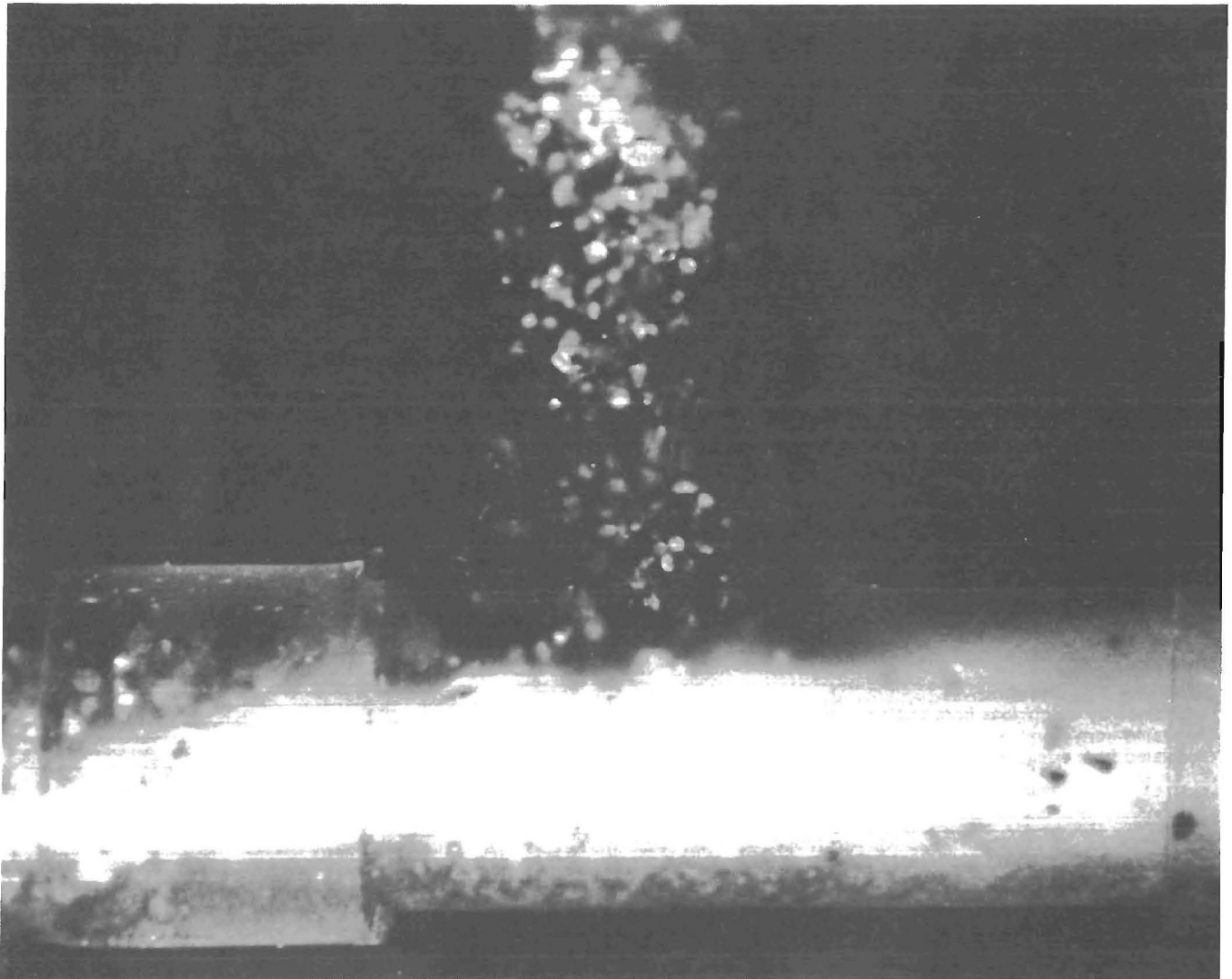


Figure 17.-Abrasive Induction into water jet.

Induction Flows

Abrasive flow through polyurethane and rubber induction hoses generated static charges around the hose. These charges did not noticeably affect steady-state induction rates. Viewed through transparent induction hoses, abrasive flow appeared to be consistent, without noticeable particle aggregation or velocity modulation.

It was observed that wet abrasives could become trapped in the region of abrupt expansion inside the collimating pipe near the nozzle. When wet abrasives occupied space near the nozzle, minor reductions in induction flow rates and in line vacuum readings were noted.

Wear to Collimating Pipes

Wear due to abrasive interactions was shown to limit the operating life of steel collimating pipes. No wear was

attributed to operating without abrasives. With accurate initial alignment of nozzle and collimating pipe, half-inch-nominal ANSI schedule 80 seamless black steel pipe wore at a nearly constant rate of 0.3 g/s (table 3, fig. 18) relative to the induction rate of abrasives. With a moderately constant rate of abrasive induction of 150 g/s and a fixed operating pressure of 69 MPa, the schedule 80 collimating pipes had an operating life of roughly 20 min prior to wearing through. After abrasives had worn through a collimating pipe, wear rates were altered because of changes in abrasive induction and estimated flow. ANSI schedule 160 half-inch-nominal seamless black pipe exhibited similar weight loss per time. Yielding about 25 pct longer operating use, the greater wall thickness alone should not justify the 77 pct greater cost per length. Tungsten carbide pipe showed little wear in over 10 h of use.

Table 3.—Collimating pipe wear and effects

Running time, ¹ min	Abrasive throughput, ² kg	Pipe weight, g	Weight loss rate, g/s	Collimation							
				Air and water			Air, abrasive, and water				
				Reactive force, N	Efflux velocity, ³ m/s	Efflux power, ⁴ kW	Abrasive flow, g/s	Reactive force, N	Efflux velocity, ³ m/s	Efflux power, ⁴ kW	
0	0.0	984	NAp	380	335	63.7	NAp	NAp	NAp	NAp	NAp
1	8.9	966	0.30	375	331	62.0	149	353	277	48.9	48.9
2	17.6	948	.30	379	334	63.4	145	352	277	48.8	48.8
3	26.9	930	.30	381	336	64.0	154	354	277	49.0	49.0
4	36.0	912	.30	378	334	63.0	152	354	277	49.1	49.1
5	45.1	894	.30	374	330	61.7	151	354	277	49.1	49.1
6	54.1	880	.23	376	332	62.4	150	349	274	47.8	47.8
7	63.3	862	.30	375	331	62.0	154	354	277	49.0	49.0
8	72.6	844	.30	373	329	61.4	155	350	273	47.8	47.8
9	82.0	826	.30	375	331	62.0	156	353	276	48.6	48.6
10	91.3	807	.32	375	331	62.0	155	353	276	48.7	48.7
11	100.4	789	.30	371	327	60.7	153	350	274	47.9	47.9
12	109.3	771	.30	373	329	61.4	148	352	276	48.7	48.7
13	118.3	757	.23	369	326	60.1	150	347	272	47.2	47.2
14	127.4	739	.30	373	329	61.4	151	353	277	48.8	48.8
15	136.3	721	.30	370	326	60.4	148	350	275	48.1	48.1
20	181.6	640	.27	372	328	61.1	151	347	272	47.2	47.2

NAp Not applicable.

¹Cumulative time with abrasives.

²Determined by weight loss from platform scale.

³Calculated from equation 5 in text.

⁴Calculated from equation 14 in text.

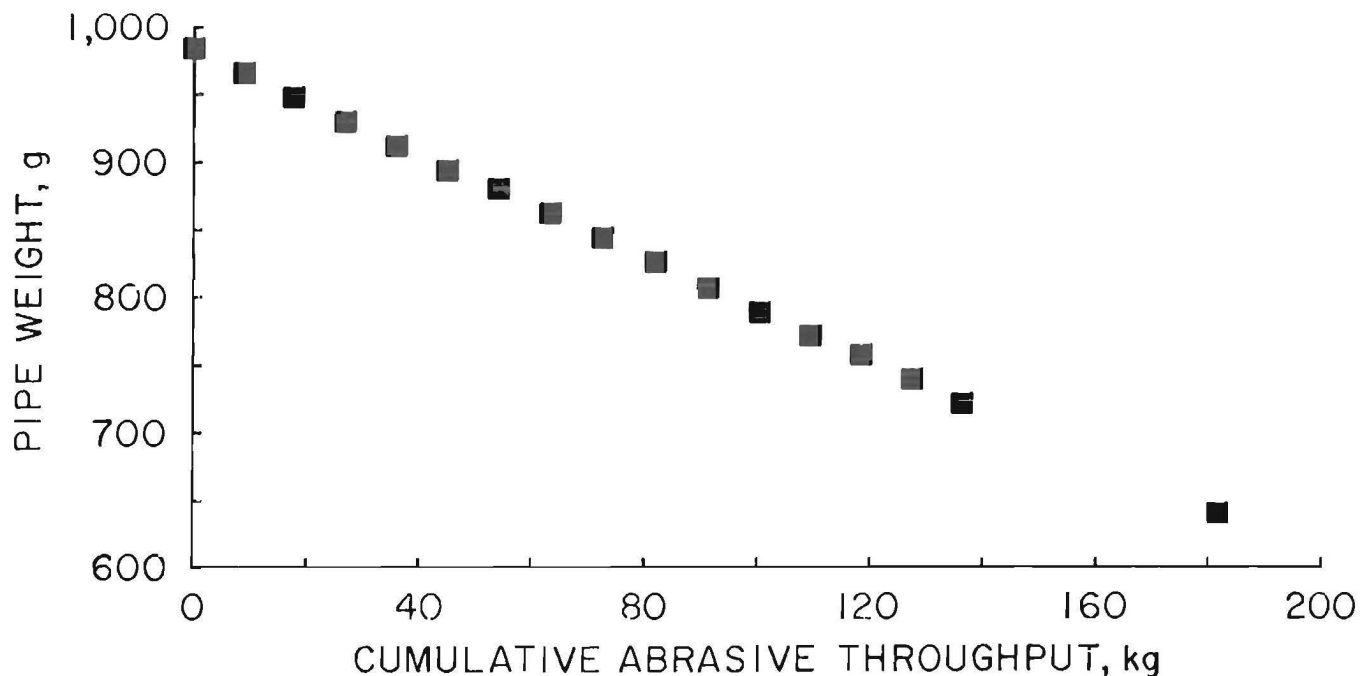


Figure 18.—Cumulative abrasive throughput versus pipe weight.

Abrasive particle collisions produced noticeable wear on both internal and external collimating pipe surfaces. Confined to the surfaces near the induction ports, external pipe wear was minor and amounted to little more than a change in the metal's finish (i.e., minute peening). The induction ports showed a greater degree of wear than the pipe exterior. After collimating pipes were sawn in half along the central axis, examination of internal surfaces

indicated that the angle of incidence of abrasive collisions with the interior pipe walls decreased with distance traveled downstream from the plane of reattachment. From measured pipe thicknesses (table 4, fig. 19), wear was shown to be greatest immediately downstream from the plane of reattachment, diminishing to minimal wear at each end.

Table 4.—Wear patterns in collimating pipes

Position, ¹ cm	Thickness, mm		Position, ¹ cm	Thickness, mm	
	Pipe A	Pipe B		Pipe A	Pipe B
0	3.72	3.78	35	1.68	2.06
5	2.88	3.06	40	2.01	2.39
10	1.84	2.15	45	2.36	2.67
15	1.00	1.69	50	2.54	2.92
20	.79	1.47	55	2.79	3.18
25	1.07	1.63	60	2.92	3.30
30	1.35	1.79			

¹Distance from influx end of collimating pipe.

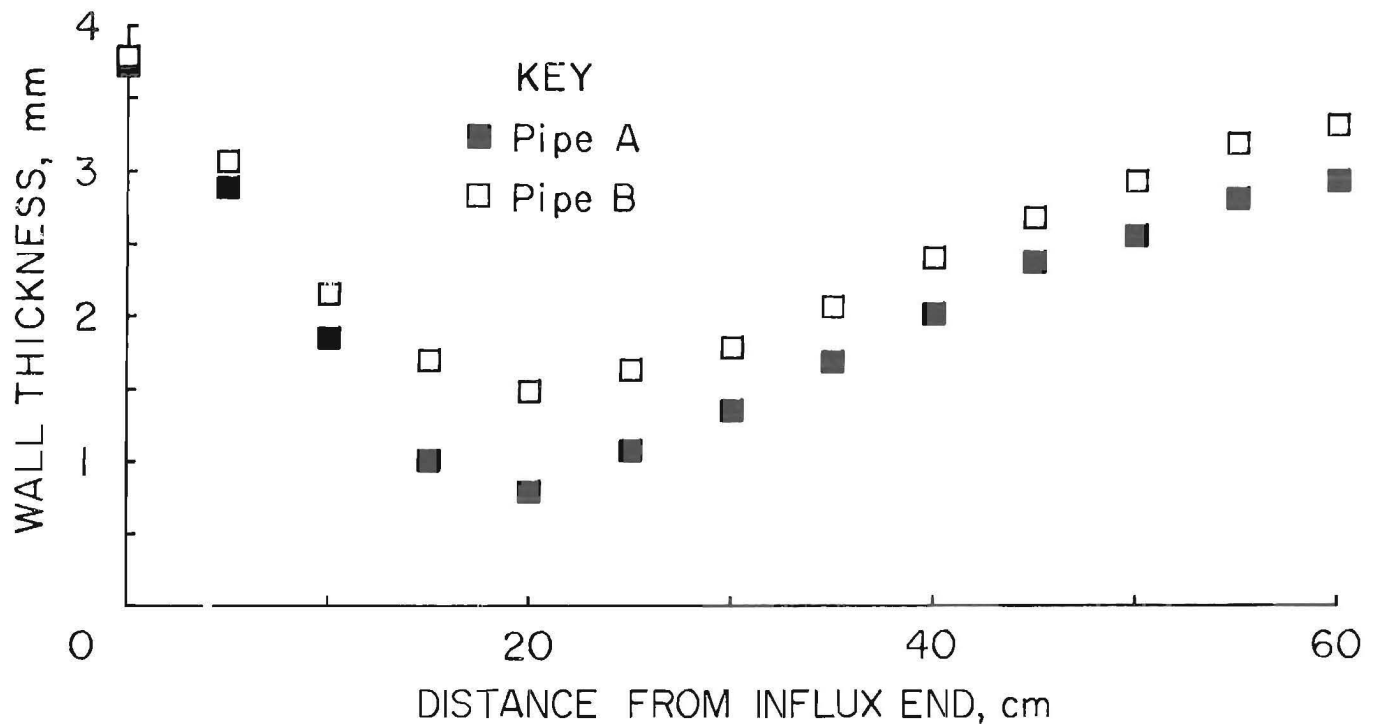


Figure 19.—Thickness profile of worn collimating pipes.

Impingement of Abrasives

Composed of individual craters, impact patterns in steel plates gave evidence of the cross-sectional distribution of particles in the jet prior to impingement. Radial distribution of impact craters is given in table 5. Impact patterns generally reflected the cross-sectional area of the jet. This indicated that particle impact trajectory was not significantly influenced by the impingement flow that radiates from the jet axis along the impinged surface of the steel plates. The distribution of craters within impact patterns appeared random for all abrasives tested at 69-MPa operating pressures. For concentric rings comprising the impact pattern area, the relative impact density (i.e., the ring's percentage of total craters divided by the ring's percentage of total area) was similar for rings within an area corresponding to the jet cross section. The relative impact density fell off rapidly beyond this area. The radial distribution of craters for 15- and 61-cm collimating lengths were similar (fig. 20). This distribution of craters indicated that abrasive mixing in the collimating pipe was substantial and was evident even for short collimating lengths.

The spherical steel shot and glass beads generated craters that, when examined under magnification, exhibited smooth surfaces analogous to plastic deformation made by a spherical indenter (fig. 21). The symmetric shape of the craters simplified their analysis.

There was strong indication that some particles impacted, rebounded, and then reimpacted the steel plate. With controlled numbers of steel shot and glass beads, typical impact patterns consisted of two crater size ranges (one approximately 2.5 times larger than the other). Large and small crater positions were somewhat intermingled, with the smaller craters tending to have a more dispersed pattern. The number of spherical particles released into the jet was accounted for by the number of larger craters, while the number of smaller craters was about half this quantity. On the basis of observed curvature, the large and small craters were judged to have been made by the same-sized indenter and the smaller impacts were concluded to be the result of reimpaction, which created shallower craters.

Table 5.-Radial distribution of impact craters

Ring designation	1	2	3	4	5	6	7	8	9	10	Total
RING MEASUREMENTS											
ID	0.00	2.54	5.08	7.62	10.16	12.70	15.24	17.78	30.32	22.86	0
OD	2.54	5.08	7.62	10.16	12.70	15.24	17.78	30.32	22.86	25.40	25.40
Median radius	0.90	2.01	3.24	4.49	5.75	7.01	8.28	9.55	10.81	12.08	8.98
Area	5.07	15.20	25.34	35.47	45.60	55.74	65.87	76.01	86.14	96.27	506.71
15.24-cm COLLIMATING PIPE WITH 1 INDUCTION PORT											
Boron carbide:											
Impacts	5	13	21	13	20	23	14	8	3	0	120
Pct of total	4.17	10.83	17.50	10.83	16.67	19.17	11.67	6.67	2.50	0	100.00
Impact density ¹	4.17	3.61	3.50	1.55	1.85	1.74	0.90	0.44	0.15	0	1.00
Silica sand (rounded):											
Impacts	9	36	54	75	81	72	56	17	6	0	406
Pct of total	2.22	8.87	13.30	18.47	19.95	17.73	13.79	4.19	1.48	0	100.00
Impact density ¹	2.22	2.96	2.66	2.64	2.22	1.61	1.06	0.28	0.09	0	1.00
Silica sand (angular):											
Impacts	39	123	218	255	303	224	141	57	8	i	1,369
Pct of total	2.85	8.98	15.92	18.63	22.13	16.36	10.30	4.16	0.58	0.07	100.00
Impact density ¹	2.85	2.99	3.18	2.66	2.46	1.49	0.79	0.28	0.03	0	1.00
Steel shot (S-390)											
Impacts	3	11	16	19	24	14	14	16	5	0	122
Pct of total	2.46	9.02	13.11	15.57	19.67	11.48	11.48	13.11	4.10	0	100.00
Impact density ¹	2.46	3.01	2.62	2.22	2.19	1.04	0.88	0.87	0.24	0	1.00
61-cm COLLIMATING PIPE LENGTH WITH 4 RADIALY SPACED INDUCTION PORTS											
Boron carbide:											
Impacts	8	52	65	90	125	86	35	14	4	0	479
Pct of total	1.67	10.86	13.57	18.79	26.10	17.95	7.31	2.92	0.84	0	100.00
Impact density ¹	1.67	3.62	2.71	2.68	2.90	1.63	0.56	0.19	0.05	0	1.00
Silica sand (angular):											
Impacts	13	38	61	103	113	96	32	4	1	0	461
Pct of total	2.82	8.24	13.23	22.34	24.51	20.82	6.94	0.87	0.22	0	100.00
Impact density ¹	2.82	2.75	2.65	3.19	2.72	1.89	0.53	0.06	0.01	0	1.00
Steel shot (S-230):											
Impacts	58	140	285	417	477	329	104	19	1	3	11,843
Pct of total	3.15	7.60	15.46	22.63	25.88	17.85	5.64	1.03	0.7	0.05	100.00
Impact density ¹	3.15	2.53	3.09	3.23	2.88	1.62	0.43	0.07	0.04	0	1.00

N/Ap Not applicable.

¹Percent of total impacts divided by percent of total area.

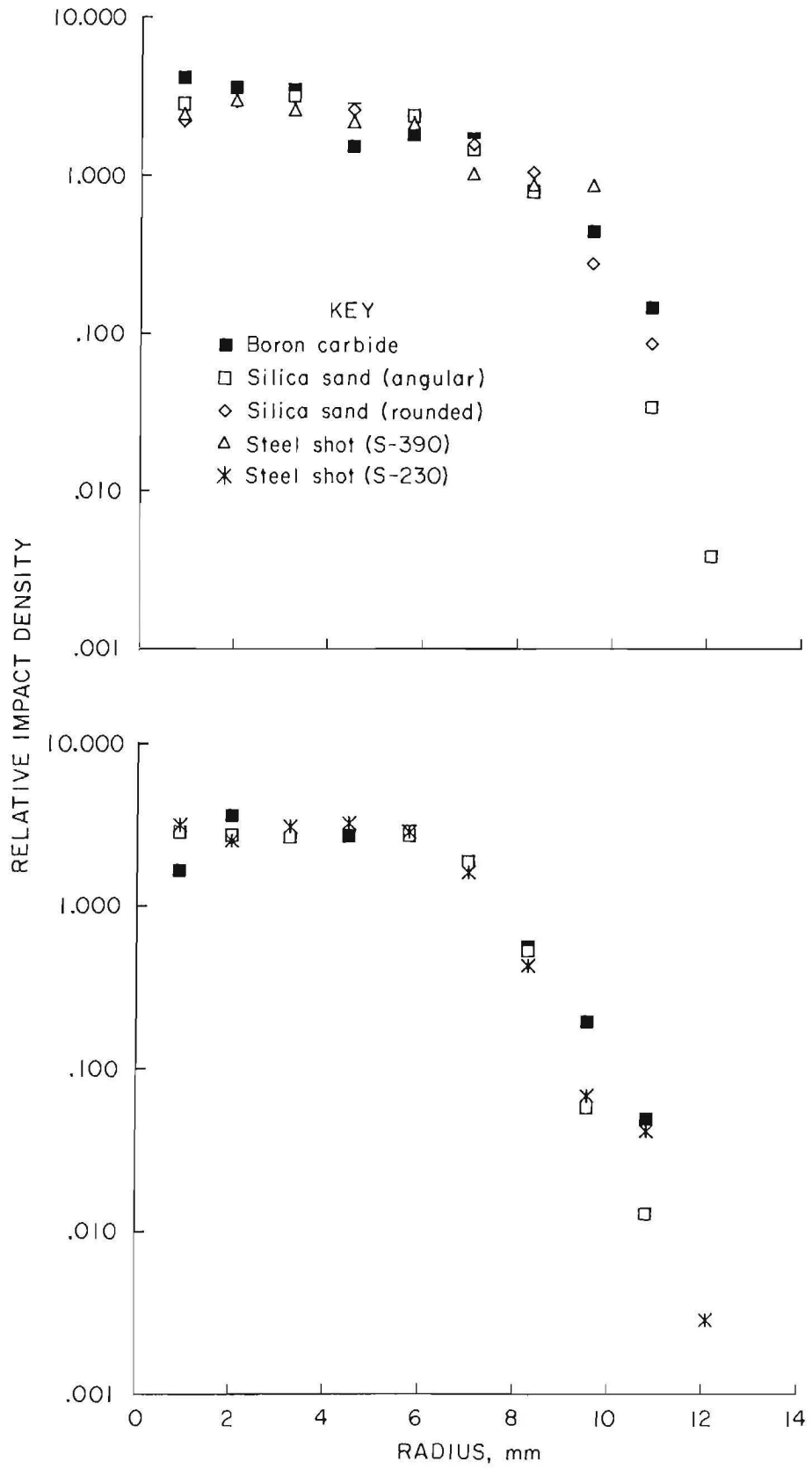


Figure 20.—Radial distribution of Impact craters. Top, using 15-cm collimating pipe with one induction port; bottom, using 61-cm collimating pipe with four induction ports.

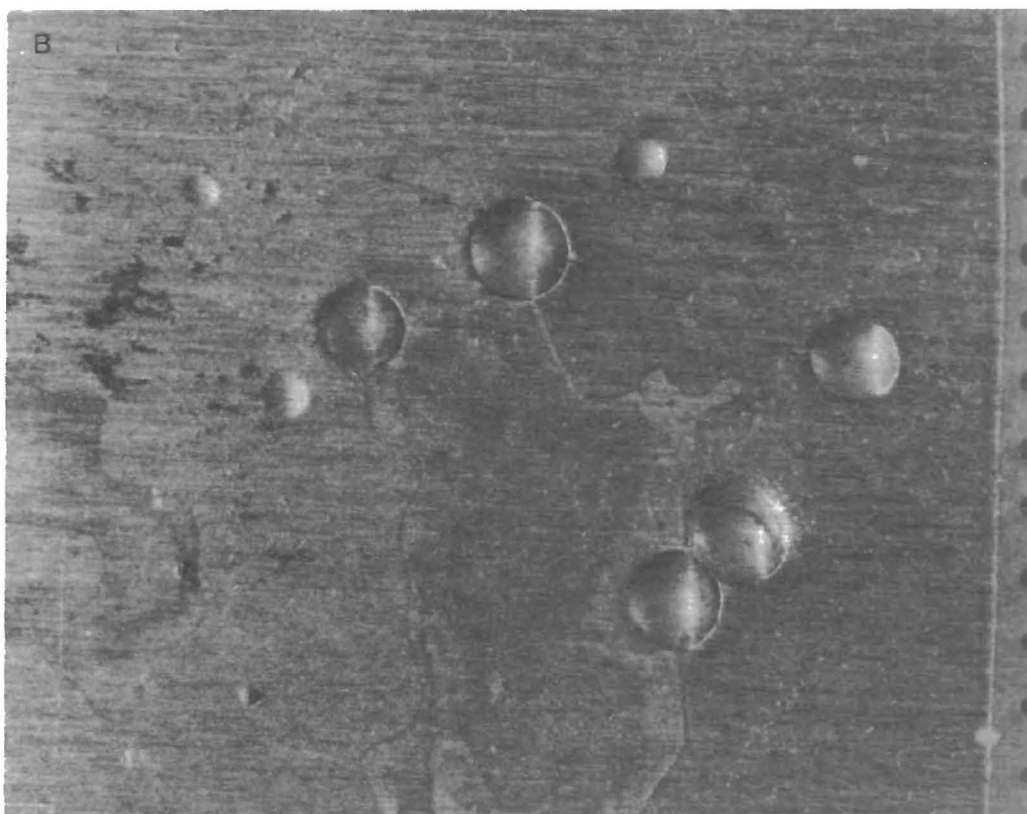
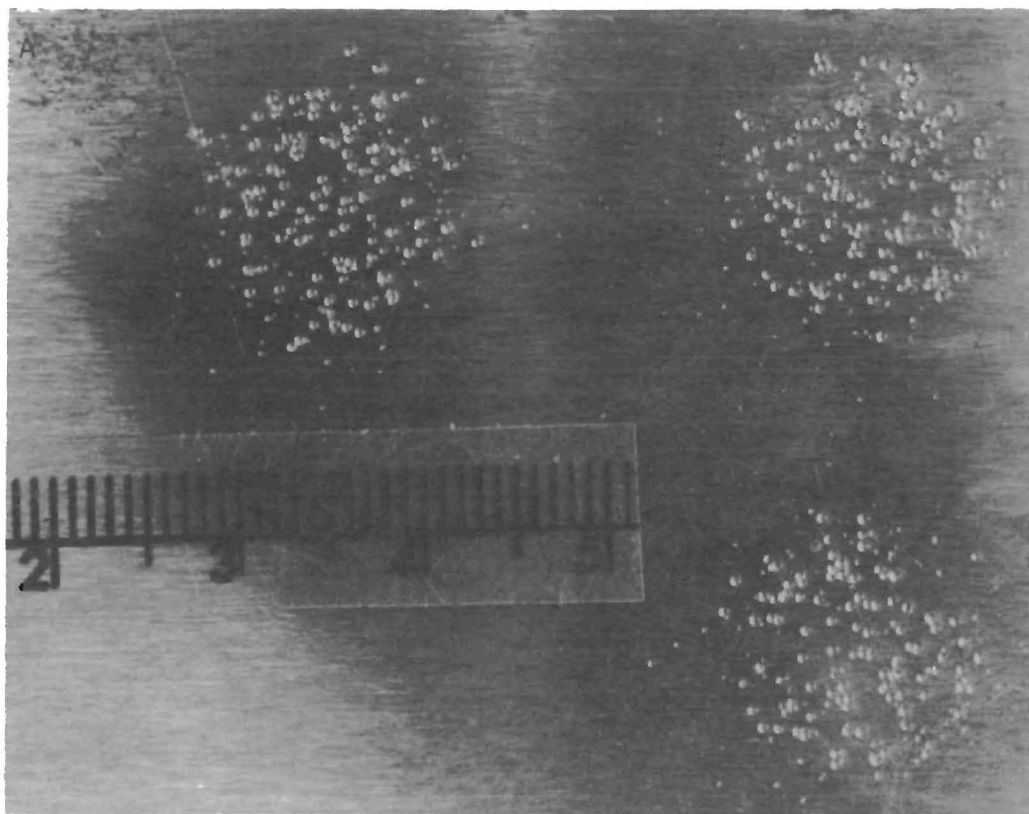


Figure 21.—Impact craters in polished steel plate. A, Using S-230 steel shot; B, using glass beads. Scale increments are in millimeters.

Crater size and position data for representative impact patterns (table 6, fig. 22) showed that the variation in crater diameter was small and that the variation had no correlation with position within the pattern. These data did not include the small craters that were concluded to have resulted from reimpaction. The small variation in crater size indicated that there was little variation in impact velocity. Hence, there was little cross-sectional variation in the velocity of abrasive particles within the jet.

Further analysis of impact craters gave a rough indication of impact pressure and particle force during impact. The smoothness of the impact crater walls indicated that

the yield strength of the ASTM A-36 steel plate had been exceeded. Using equation 16, impact pressure of 794 MPa was calculated for the 248-MPa yield-strength steel plates. The impact craters produced by the glass beads met the criterion of equation 16: the ratio of indentation diameter to indenter diameter is about 0.4. Based on an average impact area of 1.72 mm², maximum impact force for a single glass bead was estimated to be 1,370 N, by multiplying the impact pressure by area. Maximum impact force for the S-230 steel shot could not be determined because of excessive penetration.

Table 6.—Crater size data, in millimeters, using S-230 steel shot

Crater	Diameter		Av ¹	Radial position ²	Crater	Diameter		Av ¹	Radial position ²
	X-axis	Y-axis				X-axis	Y-axis		
Pattern 1:					Pattern 1—Con.				
1	0.57	0.57	0.57	8.01	48	0.54	0.56	0.55	4.51
2	.58	.56	.57	6.55	49	.65	.60	.63	7.42
3	.59	.55	.57	6.11	50	.64	.58	.61	6.84
4	.51	.50	.50	5.68	51	.54	.54	.54	5.68
5	.57	.58	.57	5.68	52	.55	.55	.55	6.26
6	.56	.58	.57	5.53	53	.46	.46	.46	7.13
7	.60	.59	.59	5.24	54	.52	.57	.55	6.99
8	.54	.54	.54	4.66	55	.52	.56	.54	6.55
9	.60	.61	.60	4.22	56	.51	.51	.51	6.55
10	.59	.57	.58	4.51	57	.54	.53	.54	7.57
11	.62	.54	.58	4.95	Av	.55	.55	.55	4.54
12	.58	.53	.56	4.08	Std. dev	.05	.05	.05	1.81
13	.55	.55	.55	3.35	Pattern 2:				
14	NAP	NAP	NAP	3.78	1	.56	.58	.57	7.57
15	.54	.53	.54	3.78	2	.47	.48	.47	7.28
16	.52	.63	.57	5.09	3	.52	.50	.51	6.26
17	.63	.59	.61	5.53	4	.55	.56	.55	5.39
18	.58	.63	.60	2.62	5	.55	.56	.56	5.53
19	.57	.56	.57	6.26	6	.55	.57	.56	6.40
20	.59	.58	.59	4.95	7	.57	.54	.55	7.13
21	.52	.51	.52	2.04	8	.55	.57	.56	6.84
22	.49	.65	.57	4.66	9	.52	.52	.52	8.73
23	.65	.64	.65	2.04	10	.54	.58	.56	6.84
24	.52	.57	.54	2.33	11	.59	.61	.60	4.66
25	.56	.50	.53	2.04	12	.53	.58	.56	4.08
26	.45	.46	.45	1.02	13	.57	.56	.57	3.49
27	.49	.50	.49	1.02	14	.59	.57	.58	3.49
28	.55	.52	.54	4.37	15	.50	.48	.49	2.18
29	.48	.47	.47	0.73	16	.51	.50	.51	1.75
30	.55	.55	.55	1.60	17	.54	.49	.52	1.89
31	.58	.54	.56	2.18	18	.53	.53	.53	1.89
32	.61	.48	.55	5.82	19	.53	.46	.50	2.33
33	.53	.45	.49	5.09	20	.54	.55	.54	2.04
34	.47	.45	.46	4.95	21	NAP	NAP	NAP	1.75
35	.52	.54	.53	2.18	22	.56	.59	.57	1.31
36	.57	.58	.58	1.75	23	.44	.45	.44	.87
37	.60	.58	.59	4.51	24	.49	.53	.51	.73
38	.46	.48	.47	4.66	25	.54	.59	.57	.58
39	.46	.44	.45	2.33	26	.56	.58	.57	1.46
40	.50	.55	.53	4.22	27	.54	.53	.53	1.89
41	.54	.56	.55	3.64	28	.63	.54	.59	2.91
42	.46	.46	.46	5.53	29	.47	.46	.46	3.20
43	.54	.52	.53	4.37	30	.51	.54	.52	4.08
44	.52	.55	.54	4.08	31	.51	.54	.52	3.93
45	.56	.56	.56	4.08	32	.59	.51	.55	1.16
46	.64	.61	.63	5.68	33	.49	.49	.49	5.53
47	.55	.53	.54	5.53	34	.56	.48	.52	6.26

See notes at end of table.

Table 6.-Crater size data, in millimeters, using S-230 steel shot-Continued

Crater	Diameter			Radial position ²	Crater	Diameter			Radial position ²
	X-axis	Y-axis	Av ¹			X-axis	Y-axis	Av ¹	
Pattern 2-Con.					Pattern 3:				
35	0.58	0.58	0.58	8.15	1	1.65	1.48	1.56	4.08
36	.52	.54	.53	4.80	2	1.47	1.34	1.40	2.77
37	NAP	.57	NAP	4.37	3	1.47	1.36	1.41	4.51
38	NAP	NAP	NAP	4.22	4	1.52	1.49	1.50	5.24
39	.54	.59	.57	3.64	5	1.52	1.57	1.55	4.80
40	.53	.59	.56	4.80	Pattern 4:				
41	.52	.59	.56	4.51	1	1.46	1.50	1.48	3.06
42	.50	.53	.52	5.09	2	1.51	1.53	1.52	2.91
43	.56	.54	.55	5.82	3	1.37	1.30	1.33	4.22
44	.54	.55	.55	5.24	4	1.27	1.29	1.28	3.78
45	.53	.54	.53	3.06	5	1.51	1.50	1.51	4.22
46	.57	.56	.56	2.91	Pattern 5:				
47	.48	.47	.48	2.33	1	1.56	1.56	1.56	6.40
48	.58	NAP	NAP	2.04	2	1.62	1.49	1.56	3.20
49	.50	NAP	NAP	2.62	3	1.47	1.49	1.48	6.70
50	NAP	.61	NAP	5.09	4	1.61	1.51	1.56	4.22
51	.62	.59	.60	4.51	5	1.35	1.46	1.40	4.51
52	.58	.59	.59	5.09	Pattern 6:				
53	.59	.55	.57	4.37	1	1.45	1.49	1.47	4.95
54	.58	.61	.60	3.35	2	1.55	1.52	1.54	2.18
55	.59	.60	.60	5.24	3	1.47	1.54	1.50	2.18
56	.64	.61	.62	5.68	4	1.42	1.51	1.46	3.64
57	.59	.55	.57	5.82	5	1.45	1.44	1.45	4.076
Av	.54	.54	.54	4.34	Av ³	1.49	1.47	1.48	4.08
Std. dev	.05	.05	.05	1.91	Std. dev. ³	.09	.08	.08	1.21

NAP Not applicable.

¹Average of X-axis and Y-axis values.

²Distance from center of crater to center of pattern.

³Includes data for patterns 3-6.

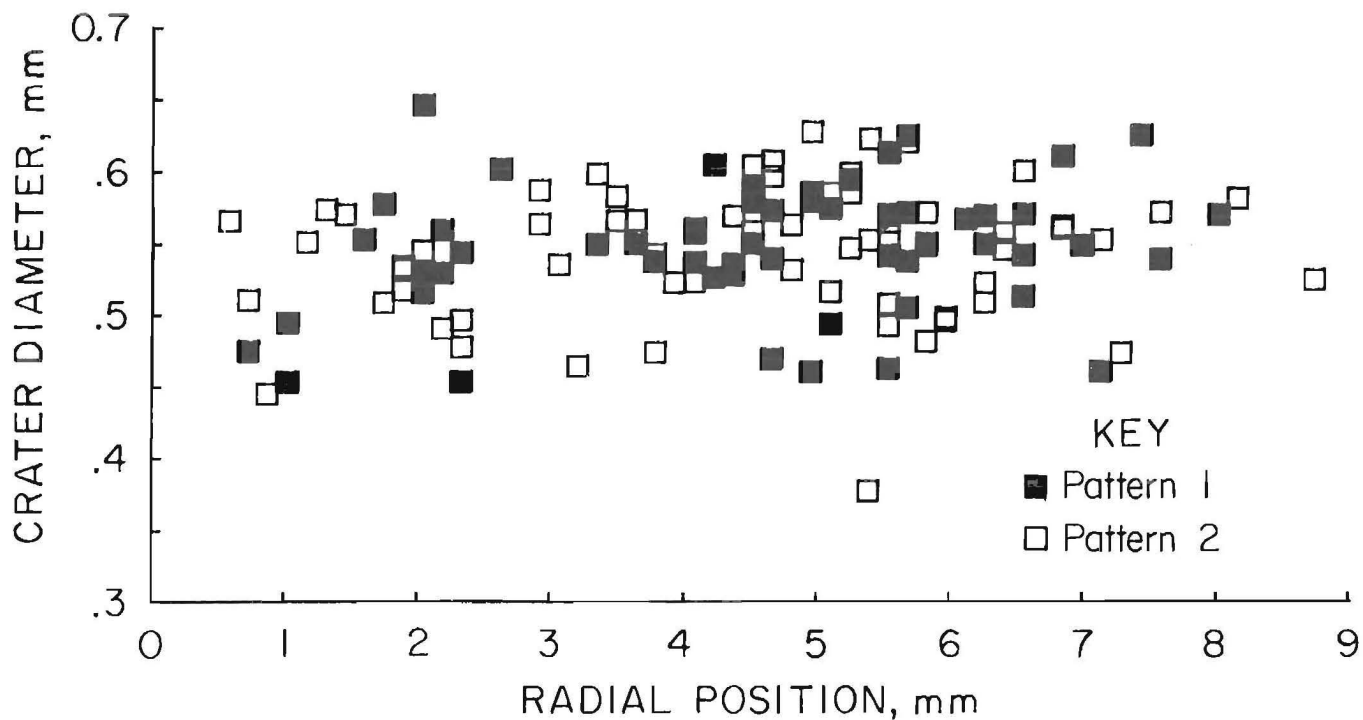


Figure 22.-Radial position versus size of impact craters.

RESPONSE TO INDEPENDENT VARIABLES

Nozzle Pressure

The nozzle discharge response to changes in operating pressure, determined without entrainment or collimating hardware, represents a no-flow-loss reference from which collimated jets may be evaluated. Flow rate, reactive force, velocity, and efflux power were determined at each

pressure level (table 7). Figure 23 gives operating pressure versus nozzle discharge rate.

For collimated flows, response data for various operating pressures were determined using 61-cm-long, 1.387-cm-ID collimating pipes in the entrainment apparatus shown in figure 12. These data (tables 8-10) include operation without induction, induction of only air, and induction of both air and abrasives.

Table 7.—Operating pressure and nozzle discharge properties

Median pump pressure MPa	Nozzle pressure, ¹ MPa	Water-flow ² kg/s	Reactive force, N	Efflux velocity, ³ m/s	Efflux power, ⁴ kW	Median pump pressure MPa	Nozzle pressure, ¹ MPa	Water-flow ² kg/s	Reactive force, N	Efflux velocity, ³ m/s	Efflux power, ⁴ kW
4.8	4.8	0.23	17	74	0.6	27.6 . . .	27.3	0.70	157	224	17.5
5.2	5.2	.24	18	76	.7	28.3 . . .	28.0	.71	159	225	17.9
5.5	5.5	.30	28	94	1.3	32.8 . . .	32.5	.77	186	244	22.7
6.2	6.1	.30	28	94	1.3	33.1 . . .	32.8	.77	187	244	22.8
8.3	8.2	.35	38	110	2.1	37.2 . . .	36.8	.82	212	260	27.5
8.6	8.5	.35	38	110	2.1	43.4 . . .	43.0	.88	249	282	35.1
9.7	9.6	.40	51	127	3.2	48.3 . . .	47.8	.93	278	297	41.3
11.0	10.9	.41	53	130	3.5	54.4 . . .	53.9	.99	313	316	49.4
13.1	13.0	.47	69	148	5.1	58.6 . . .	68.0	1.04	345	331	57.0
15.9	15.7	.53	88	167	7.4	60.7 . . .	60.1	1.06	355	336	59.7
17.2	17.0	.53	90	169	7.6	67.6 . . .	67.0	1.11	395	354	69.9
19.3	19.1	.58	109	186	10.1	68.3 . . .	67.6	1.12	396	355	70.3
20.0	19.8	.59	112	189	10.6	69.6 . . .	69.0	1.13	406	359	72.9
24.1	23.9	.64	132	205	13.5	70.3 . . .	69.7	1.14	416	364	75.7

¹Determined by subtracting head loss from pump pressure using equation 1 in text.

²Calculated from equation 6 in text.

³Calculated from equation 5 in text.

⁴Calculated from equation 14 in text.

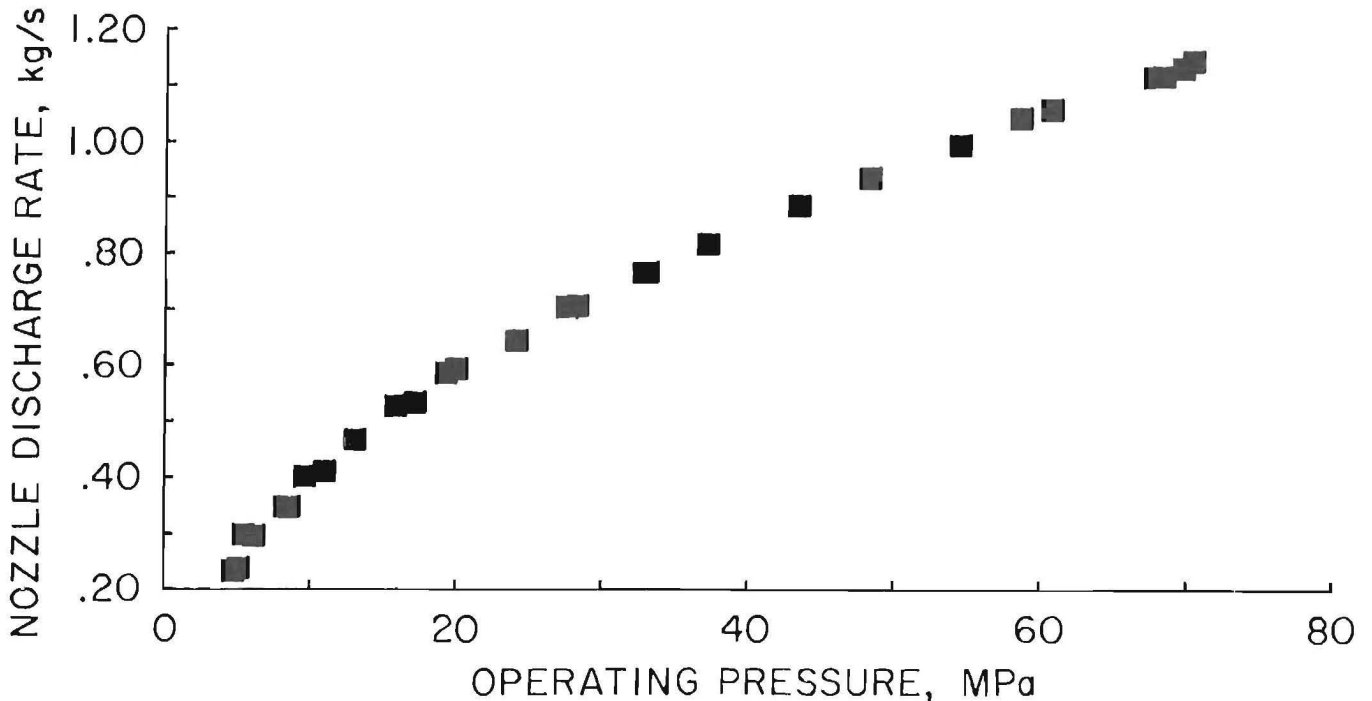


Figure 23.—Operating pressure versus nozzle discharge rate.

Table 8.—Operating pressure and collimated water-jet properties (no induction)

Median pump pressure, MPa	Nozzle pressure, ¹ MPa	Nozzle efflux velocity, ² m/s	Water-flow, ³ kg/s	Induction line vacuum, kPa	Pipe reactive force, N	Pipe efflux velocity, ⁴ m/s	Pipe efflux power, ⁵ kW
5.5	5.4	94.4	0.30	72.7	12	40	0.2
17.3	17.1	170.2	.53	93.8	67	125	4.2
34.4	34.1	249.9	.78	93.8	165	210	17.3
51.8	51.3	307.9	.97	93.8	277	286	39.7
69.0	68.4	357.4	1.12	93.4	359	320	57.4

¹Determined by subtracting head loss from pump pressure using equation 1 in text.

²Interpolated from table 7, efflux velocity.

³Interpolated from table 7, waterflow.

⁴Calculated from equation 5 in text.

⁵Calculated from equation 14 in text.

Table 9.—Operating pressure and collimated water-jet properties (air induction)

Median pump pressure, MPa	Nozzle pressure, ¹ MPa	Water-flow, ² kg/s	Induction line vacuum, kPa	Induction air density, ³ g/L	Air-flow, ⁴ g/s	Pipe reactive force, N	Pipe efflux velocity, ⁵ m/s	Pipe efflux power, ⁶ kW
6.9	6.8	0.31	1.2	1.2	7.2	25	78	1.0
13.8	13.7	.48	7.5	1.1	8.8	60	122	3.7
20.7	20.5	.60	7.8	1.1	9.8	95	155	7.4
27.6	27.3	.70	8.1	1.1	10.2	130	182	11.9
34.5	34.2	.78	8.5	1.1	10.7	170	214	18.2
41.4	41.0	.86	8.6	1.1	10.7	215	246	26.5
48.3	47.8	.93	8.8	1.1	10.7	250	264	33.1
55.2	54.7	1.00	9.1	1.1	10.7	290	287	41.6
62.1	61.5	1.07	9.4	1.1	10.6	340	315	53.6
69.0	68.4	1.12	9.8	1.1	11.1	374	330	61.7

¹Determined by subtracting head loss from pump pressure using equation 1 in text.

²Interpolated from table 7, waterflow.

³From table 2, using vacuum pressure reading and ambient conditions.

⁴Calculated from equation 4, where v was determined by anemometer measurements.

⁵Calculated from equation 5 in text.

⁶Calculated from equation 14 in text.

Table 10.—Operating pressure and collimated water-jet properties (air and abrasive induction)

Median pump pressure, MPa	Nozzle pressure, ¹ MPa	Water-flow, ² kg/s	Induction line vacuum, kPa	Induction air density, ³ g/L	Air-flow, ⁴ g/s	Abrasive flow, ⁵ g/s	Pipe reactive force, N	Pipe efflux velocity, ⁶ m/s	Pipe efflux power, ⁷ kW
6.9	6.8	0.31	7.1	1.1	1.9	110	18	42	0.4
13.8	13.7	.48	9.3	1.1	2.1	129	38	62	1.2
20.7	20.5	.60	9.3	1.1	2.1	131	76	103	3.9
27.6	27.3	.70	10.2	1.1	2.2	134	112	134	7.5
34.5	34.2	.78	9.3	1.1	2.1	126	160	176	14.0
41.4	41.0	.86	9.3	1.1	2.1	130	195	196	19.1
48.3	47.8	.93	10.2	1.1	2.3	129	230	216	24.8
55.2	54.7	1.00	10.2	1.1	2.4	124	275	244	33.6
62.1	61.5	1.07	10.2	1.1	2.3	128	330	275	45.4
69.0	68.4	1.12	10.2	1.1	2.3	130	355	283	50.2

¹Determined by subtracting head loss from pump pressure using equation 1 in text.

²Interpolated from table 7, waterflow.

³From equation in table 2, using ambient conditions.

⁴Calculated as $\delta M/\delta t = Q \cdot \rho$, where Q is determined by equation 12 and ρ is induction air density.

⁵Determined by dividing sample weight loss from platform scale by time interval.

⁶Calculated from equation 5 in text.

⁷Calculated from equation 14 in text.

With the induction flow completely restricted by a shut-off valve, vacuum gauge readings were as high as 94 kPa. With an unrestricted induction line, the induction flow rate increased with rising nozzle pressure up to a point and remained near this level for higher pressures. Induction flow rates were apparently limited by a choked flow condition. These vacuum levels are presented in figure 24.

Figure 25 contrasts reactive force, velocity, and power for the different operating conditions (i.e., operation without induction, induction of only air, and induction of both air and abrasives). The shapes of all collimated response curves were similar to their nozzle efflux counterparts. The pressure response curves for reactive force were predictably linear, while the curves for velocity and power were nonlinear. The slope of the pressure-velocity curve

decreased with increasing pressure, and the slope of the pressure-power curve increased with increasing pressure.

Comparative values were highest for the nozzle efflux flows, followed by the collimated jets with air induction, collimated jets with no induction, and lastly by the jets with induction of both air and abrasives. E.g., at 69-MPa operating pressure, a comparison of reactive forces yields 401 N for the nozzle, 359 N for collimation without induction, 374 N for collimation with only air induction, and 355 N for collimation with induction of both air and abrasives. In this case, reactive force losses relative to the nozzle efflux were 10.5 pct for collimation without induction, 6.7 pct for collimation with induction of 11.1 g/s of air, and 11.5 pct for collimation with induction of 2.3 g/s of air and 130 g/s of abrasive.

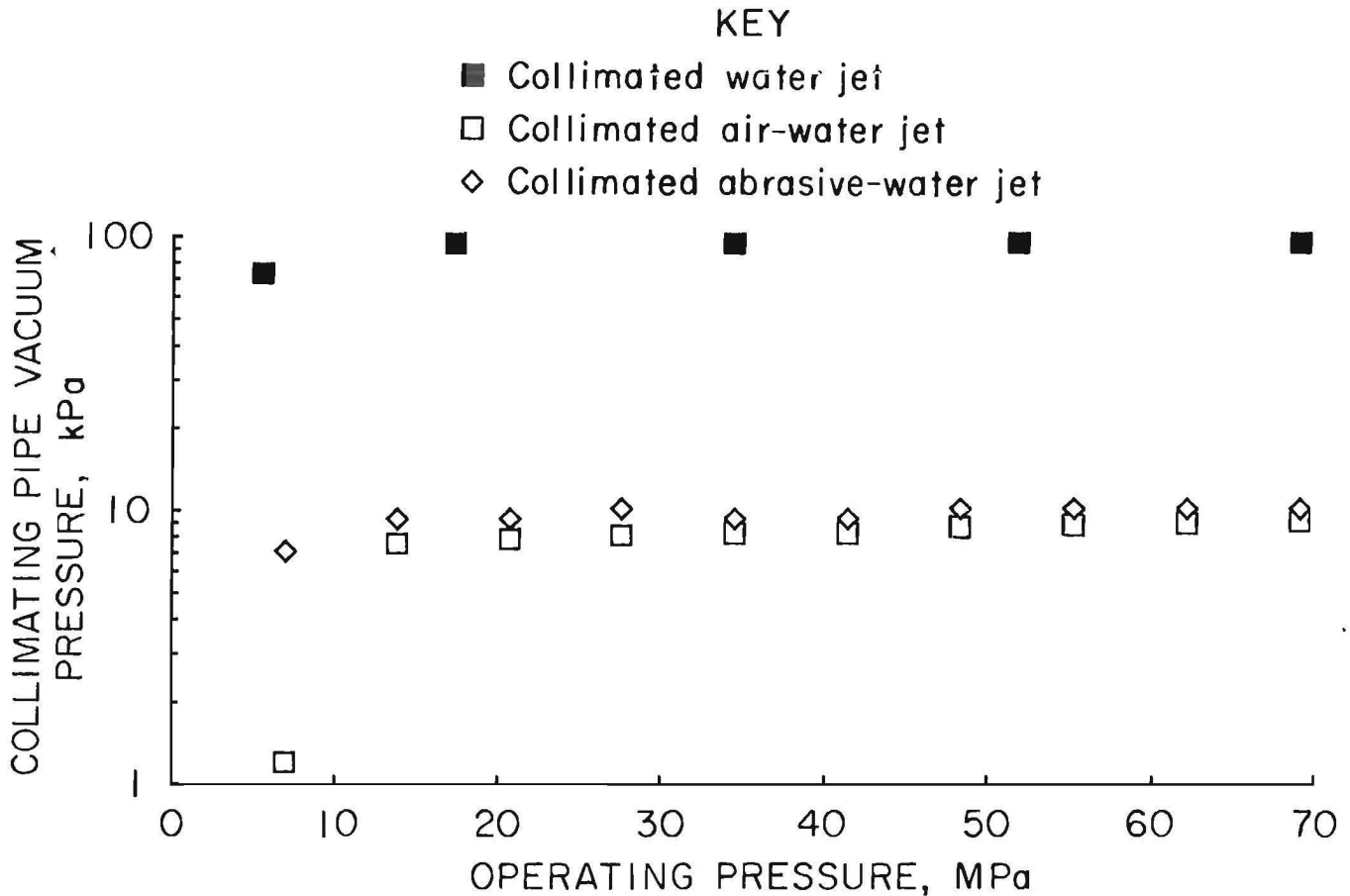


Figure 24.-Operating pressure versus induction line vacuum.

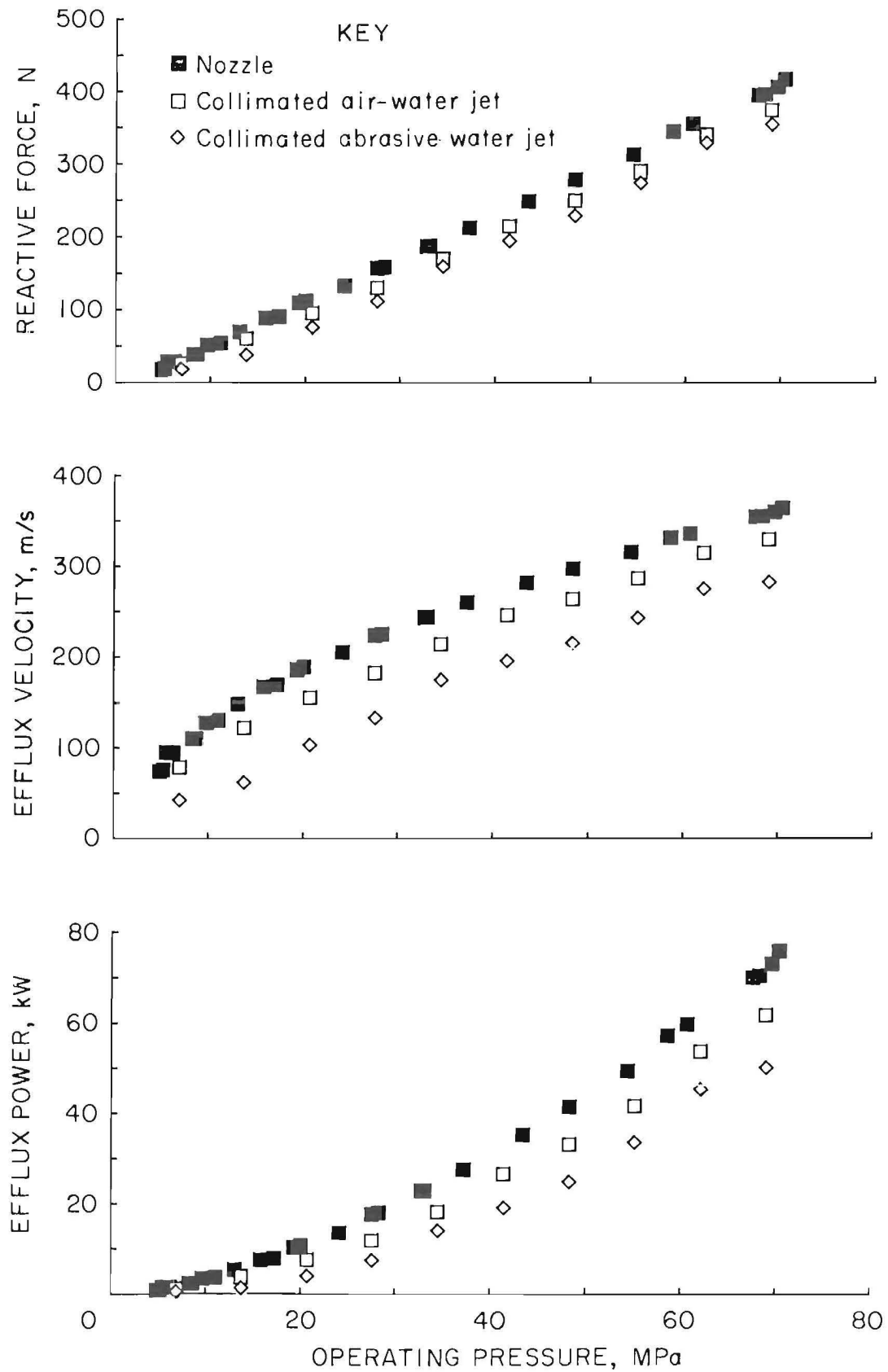


Figure 25.—Operating pressure versus reactive force, efflux velocity, and efflux power.

Table 11 gives the composition of the CAWJ by phase for various nozzle pressures. At 69-MPa pump pressure, the CAWJ was determined to be 89 pct water by weight

and 97 pct air by volume. With increasing nozzle pressure, the percentage of water by weight increased while the percentage of both air and abrasives decreased (fig. 26).

Table 11.—Collimated water-jet composition by phase

Pump pressure, MPa	Nozzle pressure, MPa	Air, wt pct	Sand, wt pct	Water, wt pct	Air, vol pct	Sand, vol pct	Water, vol pct
COLLIMATION OF WATER							
5.5	5.4	0	0	100.00	95.15	0	4.85
17.3	17.1	0	0	100.00	97.18	0	2.82
34.4	34.1	0	0	100.00	97.53	0	2.47
51.8	51.3	0	0	100.00	97.76	0	2.24
69.0	68.4	0	0	100.00	97.67	0	2.33
COLLIMATION OF AIR AND WATER							
6.9	6.8	2.24	0	97.76	97.36	0	2.64
13.8	13.7	1.79	0	98.21	97.40	0	2.60
20.7	20.5	1.60	0	98.40	97.43	0	2.57
27.6	27.3	1.44	0	98.56	97.45	0	2.55
34.5	34.2	1.35	0	98.65	97.58	0	2.42
41.4	41.0	1.23	0	98.77	97.68	0	2.32
48.3	47.8	1.13	0	98.87	97.66	0	2.34
55.2	54.7	1.06	0	98.94	97.69	0	2.31
62.1	61.5	.99	0	99.01	97.76	0	2.24
69.0	68.4	.98	0	99.02	97.75	0	2.25
COLLIMATION OF AIR, ABRASIVES, AND WATER							
6.9	6.8	0.44	25.92	73.63	94.48	0.65	4.88
13.8	13.7	.34	21.06	78.60	94.34	.52	5.14
20.7	20.5	.28	17.82	81.89	95.83	.32	3.85
27.6	27.3	.26	15.97	83.76	96.26	.25	3.48
34.5	34.2	.24	13.82	85.94	96.87	.18	2.95
41.4	41.0	.21	13.07	86.72	96.92	.17	2.91
48.3	47.8	.21	12.10	87.69	96.98	.15	2.87
55.2	54.7	.21	11.00	88.78	97.16	.13	2.71
62.1	61.5	.19	10.68	89.12	97.32	.12	2.57
69.0	68.4	.18	10.36	89.46	97.26	.11	2.63

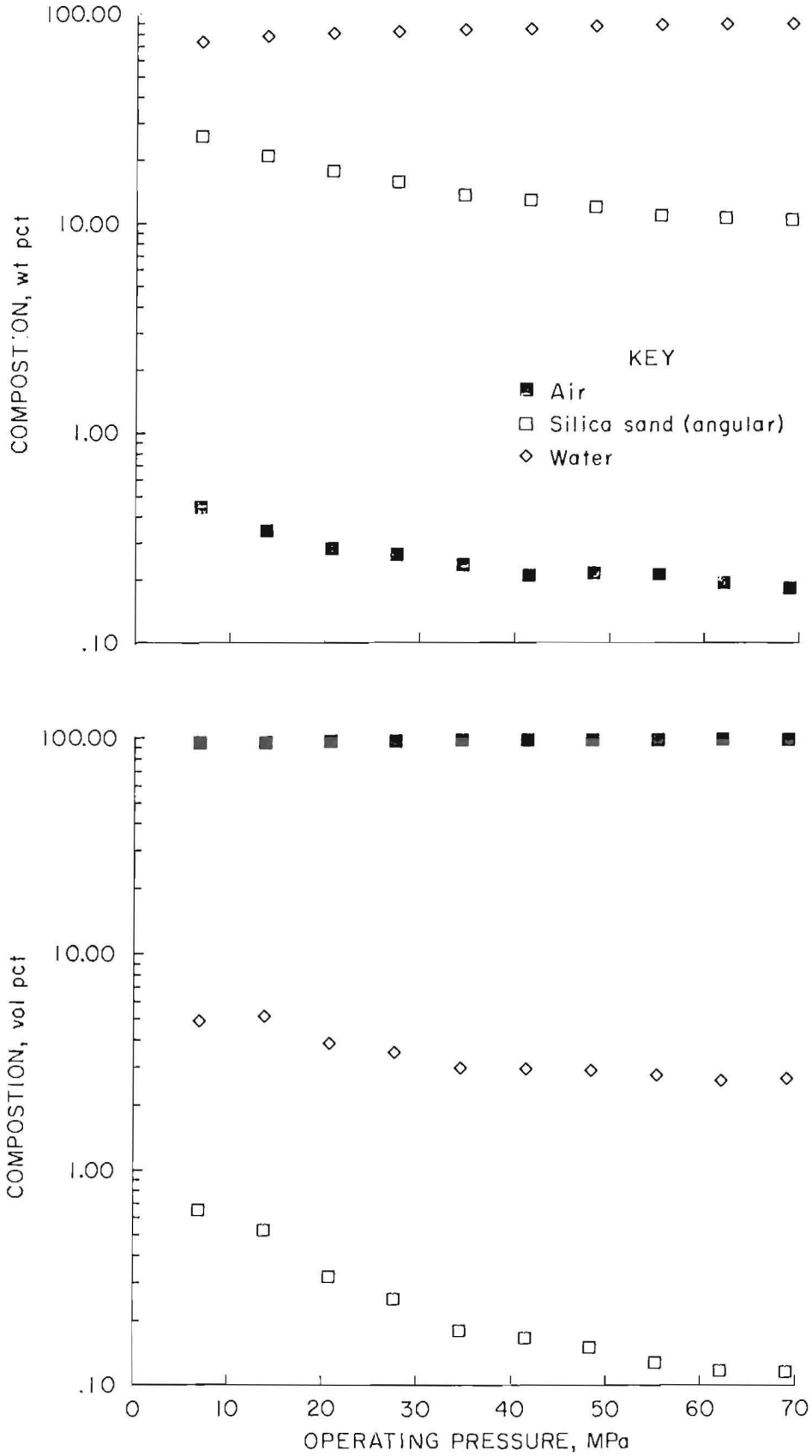


Figure 26.-Operating pressure versus composition by weight and composition by volume.

Collimating Pipe Length

For 13.9-mm-ID collimating pipes, data for a range of collimating pipe lengths are presented in table 12. Reactive force and computed flow values were not obtained for pipe lengths of less than 0.15 m or more than 3.05 m, because full collimation did not occur at the shortest lengths and because of difficulty in acquiring and maintaining straight pipes of longer lengths.

No significant change in induction rate accompanied the change in collimating pipe length from 0.15 to 3.05 m. This was the case for both air-only and abrasive induction. The apparent reason is that flow alteration downstream from the reattachment point has little effect on induction occurring near the nozzle.

Reactive force, flow velocity, and power decreased with increased collimating pipe length (fig. 27). These decreases were presumably the result of increased friction within the collimating pipe. Change in response from the shortest length to the longest length condition was greater for collimated jets with induction of both air and abrasives than with the induction of air alone. From 0.15 to 3.05 m, losses for the collimated water jet with abrasive induction and with air-only induction were 17 and 10 pct, respectively, for reactive force and velocity, and 31 and 19 pct for power. This result was contrary to the supposition that the denser mixture would better retain its inertia.

Table 12.—Collimating pipe length and collimated water-jet properties—data summary (averages)

Pipe length, m	Air and water collimation			Air, abrasive, and water collimation			
	Reactive force, N	Efflux velocity, ¹ m/s	Efflux power, ² kW	Abrasive flow, ³ g/s	Reactive force, N	Efflux velocity, ¹ m/s	Efflux power, ² kW
0.15 ..	392	344	67.5	145	379	297	56.1
0.30 ..	374	328	61.5	144	364	286	52.0
0.61 ..	372	326	60.5	147	350	274	48.0
0.91 ..	369	324	59.8	150	346	270	46.7
1.22 ..	367	322	59.2	143	337	265	44.6
1.52 ..	364	319	58.0	146	334	261	43.6
1.83 ..	362	318	57.5	140	332	261	43.3
2.13 ..	361	317	57.3	147	329	258	42.5
2.44 ..	355	311	55.4	139	317	250	39.6
2.74 ..	354	310	54.9	143	315	248	39.0
3.05 ..	353	309	54.6	141	313	246	38.5

¹Calculated from equation 5 in text.

²Calculated from equation 14 in text.

³Determined by dividing sample weight loss from platform scale by time interval.

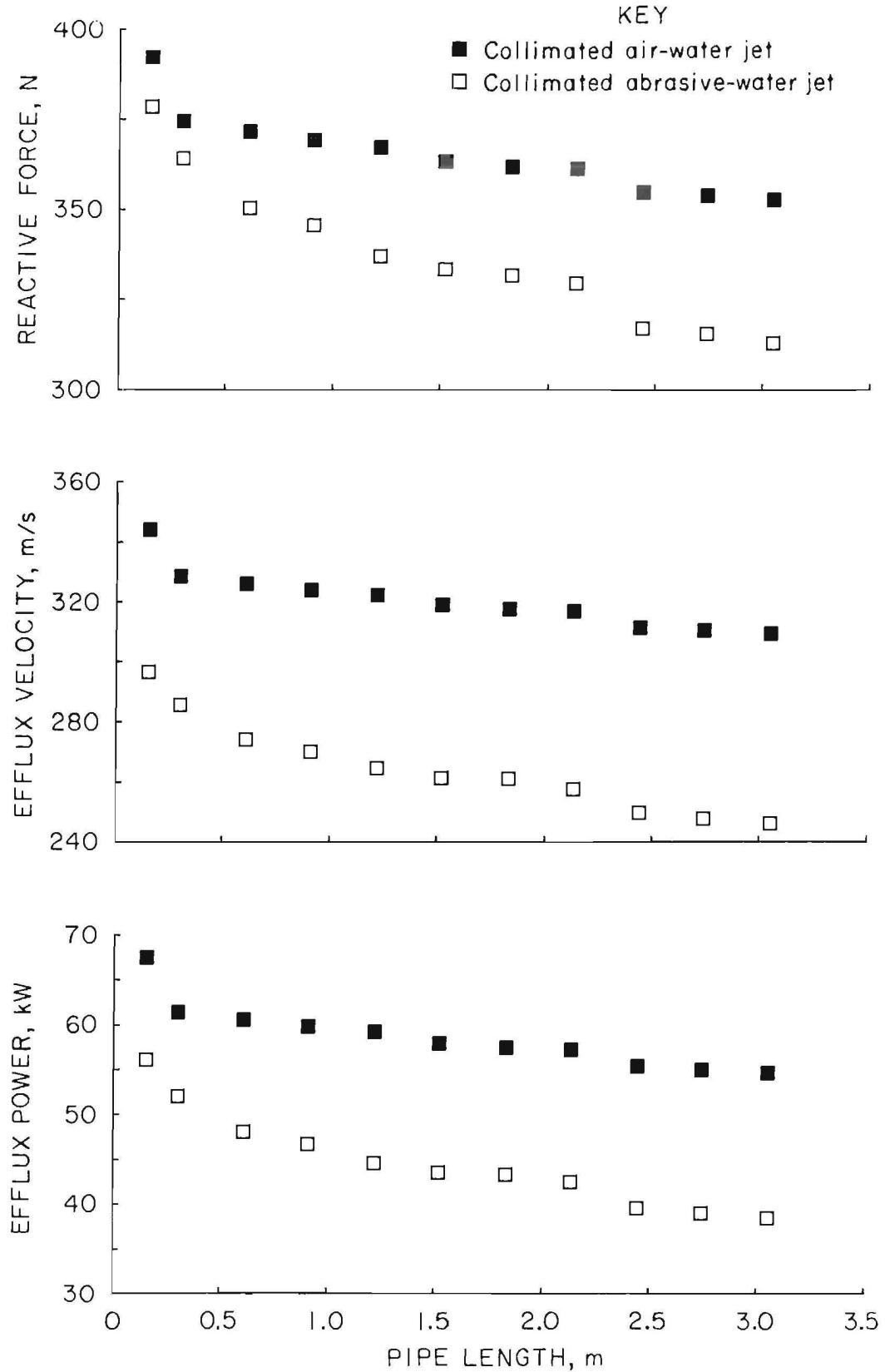


Figure 27.—Collimating pipe length versus reactive force, efflux velocity, and efflux power.

Collimating Pipe Internal Diameter

The effect of various collimating pipe diameters (table 13) was determined using 15-cm-long pipes with internal diameters of 6.4, 9.6, 12.7, and 15.9 mm at 69-MPa operating pressure. Abrasive induction rates increased significantly with increasing collimating pipe internal diameter (fig. 28). Reactive force, efflux velocity, and efflux power were affected to a modest degree by changes in collimating pipe diameter (fig. 29). Reactive force generally increased with increasing pipe internal diameter. This increase was probably due to decreased contact with surrounding walls. Efflux velocity increased minimally with increasing pipe internal diameter for flows without abrasive induction and decreased with increasing pipe internal diameter for flows

with abrasive induction. Increased abrasive entrainment for larger pipe internal diameters and, therefore, increased momentum transfer to abrasive particles accounted for the lower efflux velocities of the collimated jets with abrasives. Changes in efflux power can be explained by the respective changes in reactive thrust and velocity.

The interaction of collimating pipe inside diameter and length as independent variables was investigated by examining the conditions necessary for reattachment of the axial flow within the collimating pipe. With a 15-cm-long collimating pipe, 15.9 mm seemed to be the largest internal diameter that permitted reattachment. Presumably, longer pipes can enable collimation with larger collimating pipe internal diameters.

Table 13.-Collimating pipe internal diameter and collimated water-jet properties—data summary (averages)

Pipe ID, mm	Water collimation			Air and water collimation			Air, abrasive, and water collimation			
	Reactive force, N	Efflux velocity, ¹ m/s	Efflux power, ² kW	Reactive force, N	Efflux velocity, ¹ m/s	Efflux power, ² kW	Abrasive flow, ³ g/s	Reactive force, N	Efflux velocity, ¹ m/s	Efflux power, ² kW
6.4	379	335	63.5	390	342	64.8	80	373	307	57.1
9.6	381	337	64.2	394	345	68.5	119	381	305	58.2
12.7 . . .	379	336	63.8	396	347	69.3	145	384	301	57.7
15.9 . . .	381	338	64.3	396	348	68.9	156	381	295	56.0

¹Calculated from equation 5 in text.

²Calculated from equation 14 in text.

³Determined by dividing sample weight loss from platform scale by time interval.

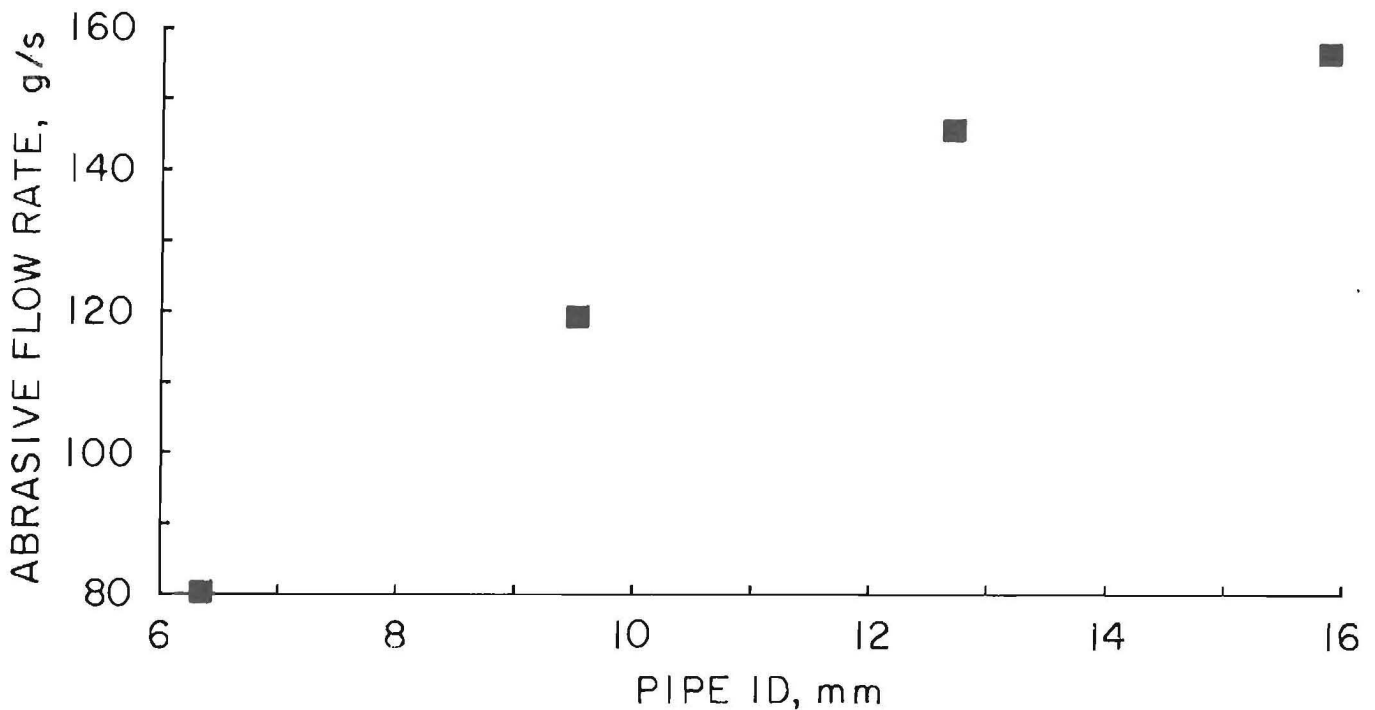


Figure 28.-Collimating pipe internal diameter versus abrasive flow rate.

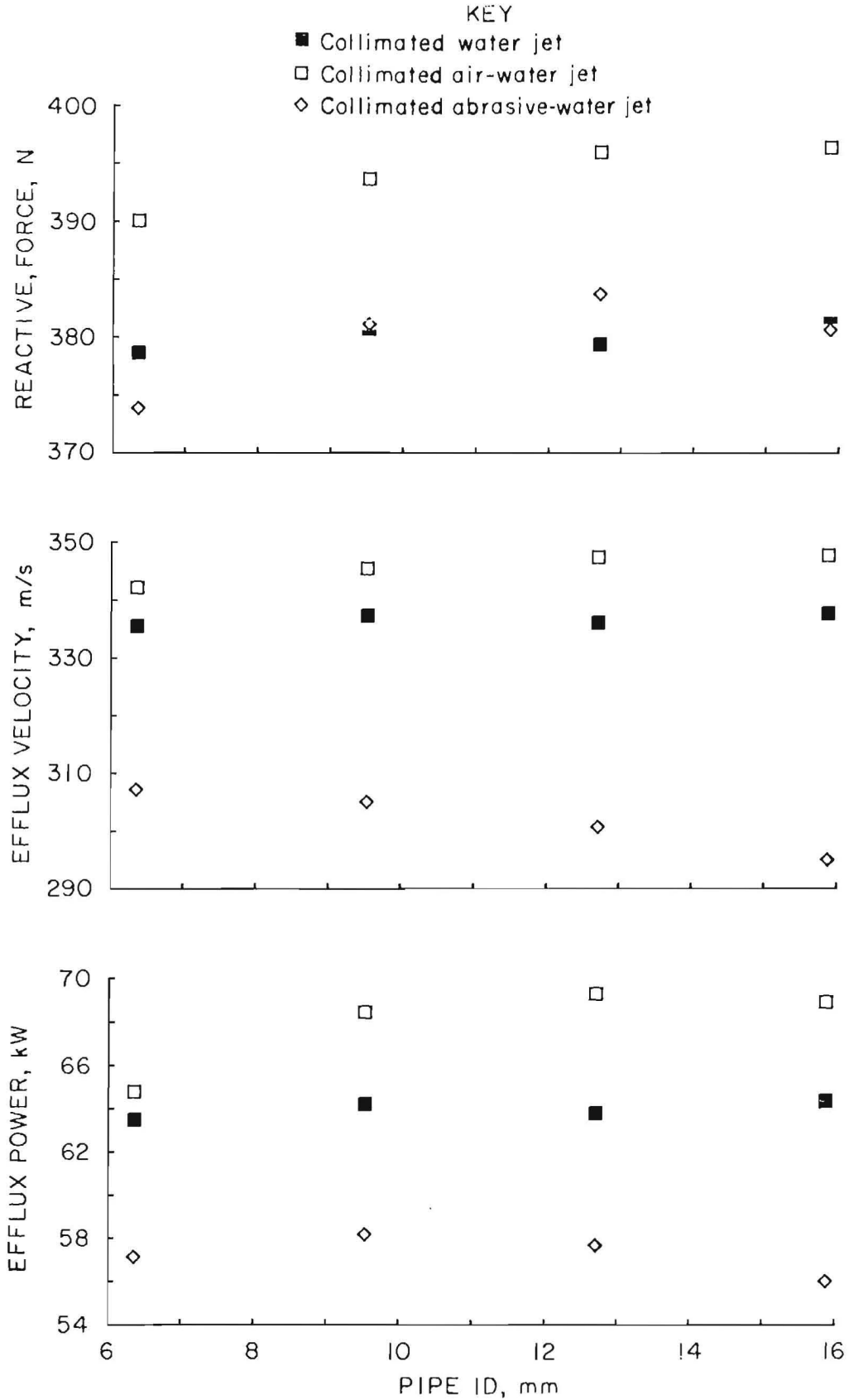


Figure 29.—Collimating pipe internal diameter versus reactive force, efflux velocity, and efflux power.

Induction Port Position and Size

Using 61-cm collimating pipes, the tested combinations of induction port location and size had mixed effects on induction rates and reactive force.

Induction rates increased as the induction port area near the nozzle increased. With total induction area held constant, no significant difference in induction rate accompanied the change from a single port to multiple ports with axis symmetry. No change was noted when the radial

orientation of the induction port in the entrainment device was changed with respect to the orientation of a single port in the collimating pipe.

No significant change in induction rate or reactive force was concluded to result from changing the axial position of induction ports between the nozzle and the reattachment plane. With 2.5-mm-ID holes drilled in the last 15 cm of a 61-cm collimating pipe, neither induction flow rates nor reactive force magnitudes were changed (table 14).

Table 14.—Induction port position and collimated water-jet properties—data summary (averages)

Duct location, ¹ cm	Air and water collimation			Air, abrasive, and water collimation			
	Reactive force, N	Efflux velocity, ² m/s	Efflux power, ³ kW	Abrasive flow, ⁴ g/s	Reactive force, N	Efflux velocity, ² m/s	Efflux power, ³ kW
1.3 . . .	369	324	59.8	152	346	269	46.5
2.5 . . .	369	323	59.6	151	345	269	46.4
5.1 . . .	368	323	59.4	156	338	262	44.3
10.2 . . .	365	320	58.5	145	343	268	46.0

¹Measured from influx end of collimating pipe.

²Calculated from equation 5 in text.

³Calculated from equation 14 in text.

⁴Determined by dividing sample weight loss from platform scale by time interval.

Alignment of Nozzle and Collimating Pipe

Axial alignment of the collimating pipe with the nozzle was important to transfer of momentum from the water jet to the abrasive particles. A 0.1-rad misalignment reduced the reactive force, decreased the exit velocity, and increased abrasive wear inside the collimating pipe. Poor alignment also changed the orientation of the reattachment plane, moving reattachment upstream on one side of the collimating pipe and downstream on the opposite side to resultantly move the point of full circumferential reattachment downstream. If the pipe was marginally long enough to enable collimation with proper alignment, misalignment prevented full collimated flow from being established.

If the collimating pipe was misaligned or too short, the expanding axial jet exited it before circumferential reattachment with it (fig. 30), and a new circulation was established with outside air flowing into the efflux end of the collimating pipe. Such flows were visually distinct because of the lack of symmetry of the efflux jet with the collimating pipe. With a competing circulation established, induction through the ports at the nozzle end of the collimating pipe was reduced. Bends in collimating pipes had an effect similar to that of misalignment. To maximize induction and mixing of abrasives into the jet, collimating pipes should be long enough to ensure that the axial flow expands to make full circumferential reattachment with the inner surface of the collimating pipe.

Collimating Pipe Material

Nonrigid tubing was tried as a collimating pipe material with negative results. Even with induction ports, 13-mm-ID polyvinyl plastic tubing with 1.6-mm wall thickness was unable to withstand low internal pressures near the nozzle and collapsed under ambient air pressure. Pinched closed, this polyvinyl tubing was cut by the water jet before mixing could be established.

Vacuum-rated polyurethane tubing had a residual coil that made centralized flow in unsupported tubing impossible. Unsupported, the tubing reacted to jet impingement by wagging and was cut by the axial water jet as tubing curvature near the nozzle became great. When straightened and held in axial alignment with the nozzle, a 61-cm-long vacuum-rated polyurethane tube was capable of collimating and conveying water jets without abrasives at 69-MPa operating pressure. Tests with abrasives were not conducted.

Alternative collimating pipe designs showed no advantage over conventional conduit. A 60-cm pipe with a single 2.5-mm-wide slot that extended 45 cm from the efflux end showed decreased efflux reactive force in comparison with conventional nonslotted pipes. Although internal flow expanded through the slot, no utility could be found for this expansion since the jet that traveled through the slot had greatly reduced velocity. A 60-cm collimating pipe, ventilated with thirty 2.5-mm-ID holes in the final 15 cm of the pipe, showed no change in reactive force over comparable nonventilated pipes.

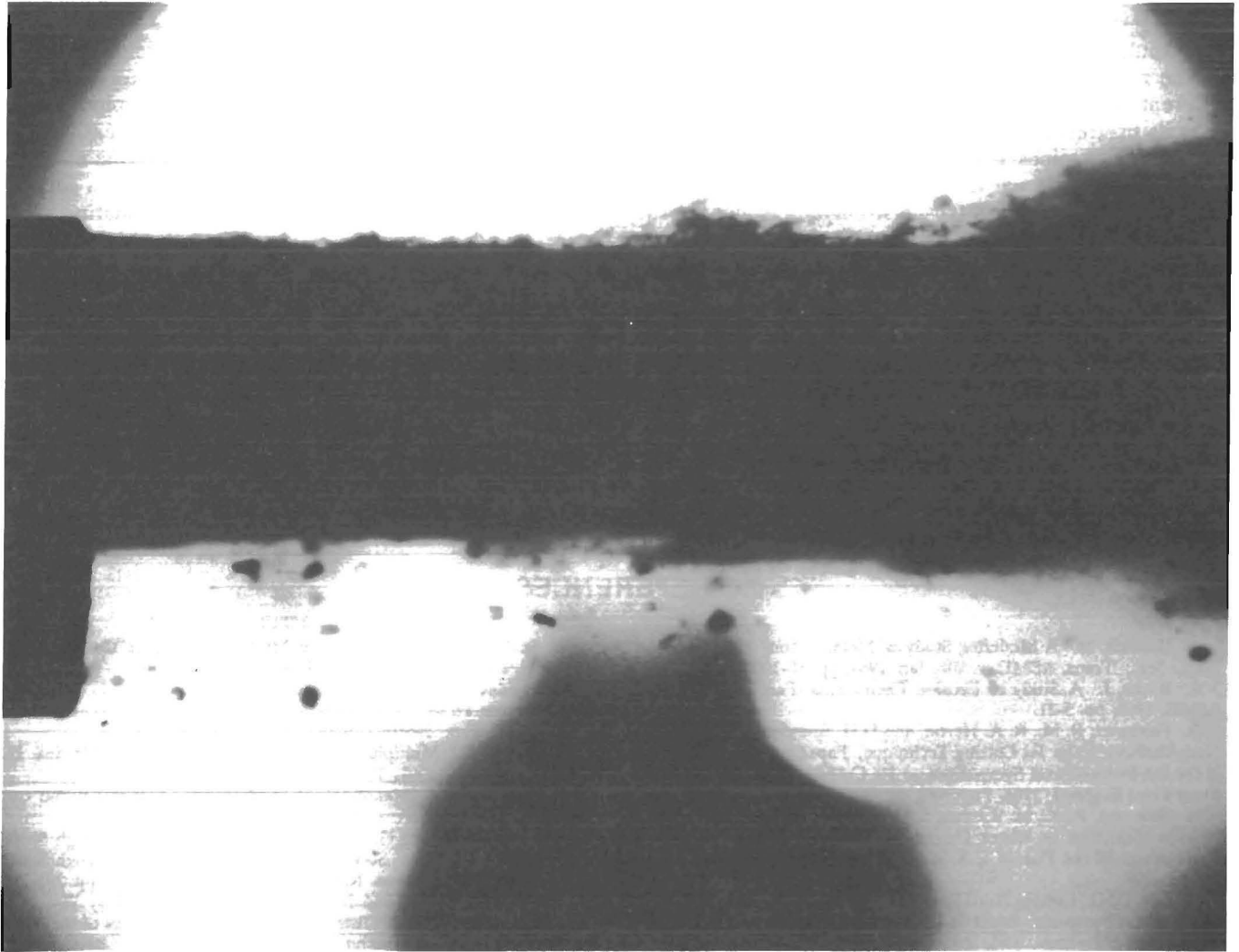


Figure 30.—Efflux flow resulting from misalignment of nozzle and collimating pipe.

DISCUSSION

Safety and design considerations arise as a consequence of the character of flow within the collimating pipe. Flow within the collimating pipe is driven by the inertia of the water that has passed through the nozzle. The flow after collimation is against a pressure gradient that increases from a partial vacuum in the induction flow to nearly atmospheric conditions at the pipe efflux.

For collimated flows, it was apparent that the volumetric flow (i.e., area times velocity) increased greatly across the mixing region while the mass flow rate remained constant. This was largely due to the approximately 10 times velocity increase from the induction line to the collimating pipe and to the fact that the internal area of the induction line nipple at 123 mm² was smaller than the collimating pipe internal area. The increase in volumetric flow rate corresponds to a decrease in internal

pressure and local expansion of air. Heat absorption from the surroundings and vaporization of water are probable consequences; however, the extent of these processes in CAWJ behavior was not investigated.

As air expanded as it traveled from the induction line into the collimating pipe, heat transfer and local cooling were indicated by ice formation. Modifications (e.g., gravity-induced abrasive flow to reduce air induction rates while maintaining abrasive flows, positive induction line pressure, or use of cryogenic fluids) may improve momentum transfer to abrasives by reducing energy dissipated through heat transfer.

Pressures inside the collimating pipe are near or below ambient atmospheric levels and the cross-sectional area of the induction line is larger than that of the nozzle orifice by orders of magnitude. For rock-cutting applications,

these are important safety considerations. In the event of a damaged or obstructed collimating pipe, the impeded flow would be safely relieved through the induction line.

The requirements for collimating pipe strength are far different from the requirements for high-pressure components upstream of the nozzle. In general, the function of collimating pipes is to provide resistance to internal collapse from external air pressure and provide confinement to the flow. High tensile strength does not appear to be a prime criterion for selection of collimating pipe materials. At this time, the recommended collimating pipe design consists of a tungsten carbide starter section followed by a replaceable section of ANSI schedule 80 seamless black pipe.

The collimating pipes used during the tests induced flow at a right angle to the main flow and provided a constant cross-sectional area throughout the region where air, water, and abrasives were mixed. Alteration of the collimating pipe design (e.g., converging and/or diverging mixing sections, and induction flows entering at another orientation) might provide improved performance.

Reduction of jet efflux velocity with collimating pipe length indicates a limitation to the practical length of collimating pipes. Because the curve was nonlinear, extrapolation of velocity with pipe length was not performed. The slope of efflux velocity versus collimating pipe length curves (deceleration curves) decreased with increasing pipe length. Practical tests are required to determine ultimate collimating pipe length limitations for cutting in a specific rock type. Because slight bends in long collimating pipes were found to reduce efflux velocity, flow losses from nonstraight pipes as well as from increased friction are likely to occur with long collimating pipes.

Because of differences in density, steel shot is less apt to mix and be collimated within the jet than siliceous abrasive of similar size and shape. However, the lack of a difference in impingement pattern between steel shot and spherical silica abrasive indicated that mixing was considerable.

REFERENCES

1. Hashish, M. A Modeling Study of Metal Cutting With Abrasive Water Jets. *Trans. ASME*, v. 106, Jan. 1984, pp. 88-100.
2. Bitter, J. A Study of Erosion Phenomena--Part 1. *Wear*, v. 6. ASME, 1963, pp. 5-21.
3. Fairhurst, R. M., R. A. Heron, and D.H. Saunders. "DIAJET"--A New Abrasive Water Jet Cutting Technique. Paper in Papers Presented at the 8th International Symposium on Jet Cutting Technology. BHRA Fluid Eng., England, 1986, Paper 40, pp. 395-402.
4. Swanson, R. K., M. Kilman, S. Cerwin, and W. Tarver. Study of Particle Velocities in Water Driven Abrasive Jet Cutting. Paper in Proceedings of the Fourth U.S. Water Jet Conference. ASME, 1987, pp. 103-107.
5. Yie, G. G. Cutting Hard Rock With Abrasive-Entrained Waterjet at Moderate Pressures. Paper in Proceedings of the Second U.S. Water Jet Conference. Univ. MO, Rolla, MO, 1983, pp. 407-420.
6. Krawza, W. G., G. A. Savanick, and S. W. Connors. End Deflector for Abrasive Water Jet Slot Cutter. U.S. Pat. 4,663,893, May 12, 1987.
7. _____. Rotatable End Deflector for Abrasive Water Jet Drill. U.S. Pat. 4,708,214, Nov. 24, 1987.
8. Savanick, G. A. and W. G. Krawza. An Abrasive Water Jet Rock Drill. Paper in Proceedings of the Fourth U.S. Water Jet Conference. ASME, 1987, pp. 129-132.
9. Savanick, G. A., W. G. Krawza, and D. E. Swanson. An Abrasive Jet Device for Cutting Deep Kerfs in Hard Rock. Paper in Third U.S. Water Jet Conference. Univ. of Pittsburgh, Pittsburgh, PA, 1985, pp. 101-122.
10. Lindeburg, M. R. Engineer in Training Review Manual. Professional Publ., San Carlos, CA, 6th ed., 1982, pp. 4-16, 19.
11. Davies, J. T. Turbulence Phenomena. Academic Press, 1972, pp. 69-72.
12. Spalding, D. B. Turbulence Models; A Lecture Course. *Imp. Coll. Sci. and Technol.*, London, U.K., Jan. 1983, p. 6.
13. Laudner, B. E., and D. B. Spalding. The Numerical Computation of Turbulent Flows. *Computer Methods in Applied Mechanics and Engineering*, v. 3. North-Holland Publ., 1974, pp. 269-289.
14. Soo, S. L. Multiphase Fluid Dynamics. Univ. IL, Urbana. IL. Preliminary revised ed., 1983, pp. 372-375.
15. Van Veen, F. Handbook of Stroboscopy. General Radio Co., West Concord, MA, Form 3163-A, 1966, p. 11.
16. Leach, S. J., and G. L. Walker. The Application of High Speed Liquid Jets to Cutting. Some Aspects of Rock Cutting by High Speed Water Jets. *Philos. Trans. R. Soc. London A*, v. 260, 1965, pp. 295-315.
17. Savanick, G. A., and J. N. Frank. Force Exerted by Water Jet Impact at Long Standoff Distances. Paper in Proceedings of the Third International Symposium on Jet Cutting Technology. BHRA Fluid Eng., England, 1976, pp. B5-B9.
18. Weast, R. C. (ed.). Handbook of Chemistry and Physics. Chemical Rubber Co., 51st ed., 1971, pp. f-9-f-10.
19. Halliday, D., and R. Resnick. *Physics*. Parts I and II. Wiley, 3d ed., 1978, pp. 392-394.
20. Lindeburg, M. R. Mechanical Engineering Review Manual. Professional Publ., San Carlos, CA, 7th ed., 1984, pp. 3-34.
21. McClintock, F. A., and A. S. Argon. Mechanical Behavior of Materials. Addison-Wesley Publ., Reading, MA, 1966, pp. 453-458.
22. Samimy, M., and A. L. Addy. The Fluid Dynamics of Safety Valve Vent Stacks. *J. Fluids Eng.*, v. 107, Sept. 1985, pp. 397-401.
23. Acar, M., R. K. Turton, and G. R. Wray. Air Flow in Yarn Texturing Nozzles. *J. Eng. Ind.*, v. 109, Aug. 1987, pp. 197-202.
24. Spalding, D. B. A Two Equation Model of Turbulence. Commemorative Lecture for Prof. F. Bosnjakovic. VDI-Forschungsh., v. 549, 1972, pp. 5-16.

APPENDIX.—SYMBOL IDENTIFICATION

A	area	M_b	Meyer ball hardness
B	barometric pressure	P	power
d	depth	p	pressure
ρ	density	Q	volumetric flow rate
D	diameter	Δp	relative pressure
δ	differential	T	temperature
F	force, applied load	t	time
b	gauge pressure, induction line	e	vapor pressure
C	Hazen-Williams constant	v	velocity
L	length	Y	yield strength
M	mass		